



KTH Engineering Sciences

On efficient and adaptive modelling of friction damping in bladed disks

Mohammad Afzal

Doctoral Thesis



Department of Aeronautical and Vehicle Engineering

KTH Royal Institute of Technology

Stockholm, Sweden 2017

Academic thesis with permission by KTH Royal Institute of Technology, Stockholm, to be submitted for public examination for the degree of Doctorate in Engineering Mechanics, Wednesday the 12th of April, 2017 at 10.00, in Room F3, Lindstedtsvägen 26, KTH–Royal Institute of Technology, Stockholm, Sweden.

TRITA-AVE 2017 : 10

ISSN 1651 – 7660

ISBN–978 – 91 – 7729 – 292 – 0

© Mohammad Afzal, 2017

Postal address:

KTH, SCI

Farkost och Flyg

SE–100 44 Stockholm

Visiting address:

Teknikringen 8

Stockholm

Contact:

mafzal@kth.se

*“Friction had been a topic of technological attention long before the dawn of science,
yet underlying mechanism is not entirely understood till today.”*

To my beloved wife, Sania Athar.

Abstract

High cycle fatigue failure of turbine and compressor blades due to resonance in the operating frequency range is one of the main problems in the design of gas turbine engines. To suppress excessive vibrations in the blades and prevent high cycle fatigue, dry friction dampers are used by the engine manufacturers. However, due to the nonlinear nature of friction contact, analysis of such systems becomes complicated.

This work focuses on the efficient modelling of friction contact and adaptive control of friction damping in bladed disks. To efficiently simulate the friction contact problem, a 3D time-discrete contact model is reformulated and an analytical expression for the Jacobian matrix is derived in parallel to the contact forces. The analytical expression drastically reduces the computation time of the Jacobian matrix with respect to the classical finite difference method, with many points at the contact interface. Therefore, it also significantly reduces the overall computation time for the solution of the equations of motion, since the formulation of the Jacobian matrix is the most time consuming step in solving the large set of nonlinear algebraic equations when a finite difference approach is employed. The developed numerical solver is successfully applied on bladed disks with shroud contact and the advantage of full-3D contact model compared to a quasi-3D contact model having uncoupled tangential motion is presented. Furthermore, presence of higher harmonics in the nonlinear contact forces is analyzed and their effect on the excitation of the different harmonic indices (nodal diameters) of the bladed disk are systematically presented. The developed numerical solver is also applied on bladed disks with strip damper and multiple friction contacts. The equations of motion are formulated in the frequency domain using the multiharmonic balance method to accurately capture the nonlinear contact forces and displacements. Moreover, the equations of motion of the full bladed disk model are reduced to a single sector model by exploiting the concept of the cyclic symmetry boundary condition for a periodic structure.

The main parameters that influence the effectiveness of friction damping in bladed disks are engine excitation order, interface parameters (normal and tangential contact stiffness and friction coefficient), relative motion at the friction interface and the normal contact load at the interface. Due to variation in the interface parameter values during operation and also these parameters are often hard to predict at the design level, the obtained friction damping in practice may differ significantly from the optimum value. Therefore, to control the normal load adaptively that will lead to an optimum damping in the system despite these variations, use of magnetostrictive actuator is proposed in this work. The magnetostrictive material that develops an internal strain under the influence of an external magnetic field is used to increase and decrease the

normal contact load at the friction interface. A linearized model of the magnetostrictive actuator is employed to characterize the magneto-elastic behavior of the actuator. A nonlinear static contact analysis of the bladed disk and the underplatform damper reveals that a change of normal load more than 700N can be achieved using a reasonable size of the actuator. This will give a very good control on friction damping once applied in practice.

Keywords: High cycle fatigue, Friction contact, Jacobian matrix, Shroud contact, Strip damper, Multiharmonic balance method, Contact stiffness, Cyclic symmetry, Nodal diameter, Magnetostrictive actuator, Magnetic field.

Sammanfattning

Högcykelutmattning av turbin- och kompressorblad på grund av resonanser i det operativa frekvensområdet är ett av de största problemen i utformningen av gasturbinmotorer. För att dämpa överdrivna vibrationer i bladen och förhindra högcykelutmattning används torrfriktionsdämpare av många tillverkare. Men på grund av den icke-linjära naturen hos friktionskontakten blir analyser av sådana system komplicerade.

Detta arbete fokuserar på effektiv modellering av friktionskontakt och adaptiv styrning av friktionsdämpning i turbinblad. För att effektivt simulera friktionskontakten omformuleras en tidsdiskret 3D kontaktmodell med en analytiskt härledd uttryck för Jacobimatrisen parallellt med kontaktkrafterna. Det analytiska uttrycket reducerar drastiskt beräkningstiden för Jacobimatrisen med avseende på klassisk finita-differensmetoden, med många punkter vid kontaktgränssnittet. Därför minskar den totala beräkningstiden för lösningen av rörelseekvationerna eftersom formuleringen av Jacobimatrisen är det mest tidskrävande steget för att lösa den stora uppsättningen av icke-linjära algebraiska ekvationer när en finita-differensmetod används. Den utvecklade numeriska lösaren tillämpas framgångsrikt på turbinblad med shroud kontakt och fördelarna med en 3D-fullkontaktmodell i jämförelse med en 3D-kvasikontaktmodell med icke-kopplad tangentiell rörelse presenteras. Vidare analyseras förekomsten av harmoniska övertoner i kontaktkrafterna och dess påverkan på olika harmoniska index (nodala diametrar) på turbinbladen presenteras systematiskt. Den utvecklade numeriska lösaren tillämpas även på turbinblad med dämpband och multipla friktionskontakter. Rörelseekvationerna formuleras i frekvensdomänen med hjälp av en multiharmonisk balansmetod för att exakt fånga de olinjära kontaktkrafterna och förskjutningarna. Dessutom är rörelseekvationerna av hela turbinbladsmodellen reducerade till en enda sektormodell genom att utnyttja konceptet med den cykliska symmetrin samt randvillkoren för en periodisk struktur.

De viktigaste parametrarna som påverkar effektiviteten av friktionsdämpningen i turbinblad är motorexcitationsordningen, gränssnittsparametrar (normal- och tangentiellkontaktstyvhet och friktionskoefficient), relativ rörelse mellan friktionsgränssnittet och normal-kontaktlasten i gränssnittet. På grund av varierande gränssnittsparametervärden under drift (vilka är svåra att prediktera i konstruktionsstadiet) kan den erhållna friktionsdämpningen i praktiken skilja sig signifikant från ett optimalt värde. För att adaptivt styra normallasten som leder till optimal dämpning av systemet, trots variationer, föreslås användning av magnetoresistiva aktuatorer. Magnetoresistiva material som utvecklar en intern spänning under påverkan av ett magnetfält används för att minska eller öka normalkontaktlasten i friktionsgränssnittet. En linjär modell av en

magnetostriktivt aktuator används för att karakterisera det magneto-elastiska beteendet på aktuatoren. Icke-linjär kontaktanalys av turbinblad och underplattform dämparen avslöjar att en förändring av normalbelastningen mer än 700 N kan uppnås med användning av en rimlig storlek på aktuatoren. Detta kommer att ge en mycket god kontroll på friktionsdämpning då den tillämpas i praktiken.

Nyckelord: högcykelutmattning, friktionskontakt, jacobimatrix, shroud-kontakt, dämpband, multiharmonisk balansmetod, kontaktstyvhet, cyklisk symmetri, nodala diametrar, magnetostriktiva aktuatorer, magnetfält.

Acknowledgements

This work has been performed at the Department of Aeronautical and Vehicle Engineering, KTH. The financial support from the Swedish Energy Agency, Siemens Industrial Turbomachinery AB, GKN Aerospace and the Royal Institute of Technology through the Swedish research program TurboPower is gratefully acknowledged.

First of all, I would like to express my deepest gratitude to my supervisors Professor Leif Kari and Professor Ines Lopez Arteaga for their professional guidance, encouragement and motivational support during this work. A special thank to Ines for on time feedbacks, discussions and correcting my mistakes during the years!

I am also thankful to Svante Finnveden for interesting discussions and help.

Further, I am also thankful to Ronnie Bladh, Vsevolod Kharyton and Maria Angelica Mayorca at Siemens Industrial Turbomachinery AB for providing me hands-on experience on DATAR software and interesting discussion about cyclic structures and friction damping.

All the colleagues and staffs at KTH, thanks for the nice company, help and discussions, especially Oskar, Rickard, Erik, Hao, Mauricio, Tobias, Salar, Danial and Maaz. In addition, I would like to thank my thesis opponent, Professor Muzio M. Gola, and other committee members, Assistant Professor Astrid Pieringer, Associate Professor Roger Johnsson and Professor Ulf Olofsson, for their interest and disposition to join the dissertation committee and I look forward to having a fruitful discussion during defense.

Finally, this work would not have been possible without the unconditional and kind support of my beloved wife and family in India.

Mohammad Afzal

Stockholm, 12th April 2017

Dissertation

This thesis consists of two parts: The first part gives an overview of the research area and work performed. The second part contains four research papers (A-D):

Paper A

M. Afzal, I. Lopez Arteaga and L. Kari, *An analytical calculation of the jacobian matrix for 3D numerical friction contact model applied to turbine blade shroud contact*, Computers & Structures 177 (2016) 204-217.

M. Afzal performed the studies and initiated the direction of research, made the analysis, the coding and produced the paper. I. Lopez Arteaga and L. Kari supervised the work, discussed ideas and reviewed the work.

Paper B

M. Afzal, V. Kharyton, I. Lopez Arteaga and L. Kari, *Investigation of damping potential of strip damper on a real turbine blade*, in: Paper GT2016-57230, Proceedings of ASME Turbo Expo 2016, June 13-17, Seoul, South Korea, 2016.

M. Afzal and V. Kharyton generated the idea. M. Afzal wrote the code, performed the analysis and produced the paper. I. Lopez Arteaga and L. Kari supervised the work, discussed ideas and reviewed the work.

Paper C

M. Afzal, I. Lopez Arteaga and L. Kari, *Numerical analysis of multiple friction contacts in bladed disks*, submitted.

M. Afzal extended the developed code, performed the analysis and produced the paper. I. Lopez Arteaga and L. Kari supervised the work, discussed ideas and reviewed the work.

Paper D

M. Afzal, I. Lopez Arteaga and L. Kari, *Adaptive control of normal load at the friction interface of bladed disks using giant magnetostrictive material*, to be submitted.

L. Kari originated the idea. M. Afzal, I. Lopez Arteaga and L. Kari scrutinized the proposal. M. Afzal performed the analysis and produced the paper. I. Lopez Arteaga and L. Kari supervised and reviewed the work.

In addition to the appended papers, the work has resulted in the following reports and presentations:

AROMA 1.0 Structural damping–Why friction matters and how we best model it?

Mohammad Afzal

Presented at *TurboPower Program Conference 2013*, Lund University of Technology, Lund, Sweden

AROMA 2.0 Structural damping–Influence of variable normal load on friction damping

Mohammad Afzal

Presented at *TurboPower Program Conference 2014*, KTH, Stockholm, Sweden

AROMA 2.0 Structural damping–Alternate frequency time domain method

Mohammad Afzal

Presented at *TurboPower Program Conference 2015*, Linköping University, Linköping, Sweden

TurboPower COMP10 final report–WP3 Structural damping

Mohammad Afzal

TurboPower Deliverable Report, Report No. COMP10-D3.4, 2015

Numerical simulation tool for friction damping

Mohammad Afzal

TurboPower Deliverable Report, Report No. COMP10-D3.5, 2015

As a part of the PhD project, the degree of Licentiate in Technology was awarded in 2015 by KTH Royal Institute of Technology to the author for the thesis “**Numerical modelling and analysis of friction contact of turbine blades.**”

Contents

I	OVERVIEW	1
1	Introduction	3
1.1	Background	3
1.2	The COMP project	7
1.3	Objectives	8
1.4	Organization of thesis	9
2	Cyclic Structures	11
2.1	Cyclic symmetric structures	11
2.2	Travelling wave excitation	12
2.3	The nonlinear equations of motion	13
2.3.1	Equations of motion of the full bladed disk	13
2.3.2	Equations of motion reduced to a single sector	14
2.3.3	Steady state solution by the multiharmonic balance method	16
2.4	Conclusion	18
3	Contact Model	19
3.1	Background review	19
3.2	Simulation results	21
3.3	Conclusion	25
4	Solution of Nonlinear Algebraic Equations	27
4.1	Receptance based method	27
4.2	Predictor step	29
4.3	Corrector step	31

CONTENTS

4.4	Step length control	31
4.5	Conclusion	33
5	Magnetostrictive Materials	35
5.1	Historical overview	35
5.2	Giant magnetostrictive material Terfenol-D	36
5.3	Adaptive control of normal load	38
5.4	Conclusion	39
6	Results	41
6.1	Test case blade	41
6.1.1	Case study-1	43
6.1.2	Case study-2	46
6.2	Real bladed disk	49
6.2.1	Case study-3	50
6.3	Conclusion	53
7	Conclusions and Recommendations for Future Work	55
7.1	Concluding remarks	55
7.2	Recommendations for future work	57
8	Summary of Appended Papers	59
	Bibliography	62
II	APPENDED PAPERS A-D	71

Part I

OVERVIEW

1 Introduction

In this chapter, a short introduction of friction damping and the aim of the research are presented. The main contributions and organization of the thesis are outlined as well.

1.1 Background

Increasing demands for low cost and efficient turbomachinery require minimization of the vibrations and stresses on the turbine blades to avoid failure of its components. Failure of turbomachinery components is very costly and may lead to substantial damage, injury and even death. Due to the high modal density of realistic turbine bladed disks and a broad frequency content of the aerodynamic excitation forces, complete prevention of the occurrence of resonance is practically infeasible. Therefore, damping of these resonances is very important. Since turbine blades do not benefit significantly from material hysteresis and aerodynamic damping; dry friction dampers, that are easy to manufacture, install, and can withstand high temperatures, are extensively used by the gas turbine engine developers to suppress excessive vibration amplitudes. Friction forces at preloaded contact interfaces dissipate vibrational energy and therefore, provide damping to the structure. Friction damping in turbomachinery is most commonly achieved by shroud coupling, underplatform dampers and root joints (Fig. 1.1).

Friction damping devices in turbomachinery applications are the subject of many research activities in past decades and numerous computational methods and experimental investigation are found in the literature. Research in the field can be broadly classified based on the following aspects:

- Modelling of structure (lumped parameter, analytical and finite element model)
- Modelling of contact interface and contact laws (macroslip vs microslip)

- Contact kinematics and computation of contact forces (time-continuous vs time-discrete)
- Solution methods

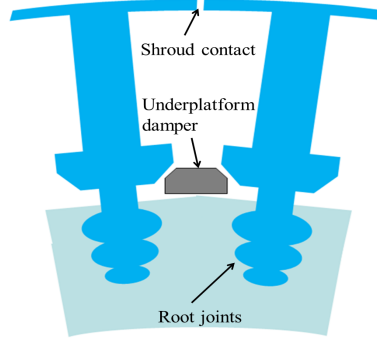


Figure 1.1: Friction damping locations.

Lumped parameter models describe the structure as a collection of rigid bodies connected by springs and dampers, disregarding the local elasticity of the structure. Some examples of these and equivalent models can be found in Refs. [1–4]. Analytical models take into account the local elasticity of the structure. Simple structures like beams and plates are accurately represented by analytical models, however they can not describe complex structures such as turbine blades. This representation is used by few researchers in the field [5, 6]. A better alternative is finite element models (FEM) that accurately represent the dynamics of complex structures [7–10]. This is essential for turbomachinery blades since they exhibit three-dimensional profile optimized for desired aerodynamic efficiency. However, the solution of nonlinear equations of motion (EQM) with a large number of degree of freedoms (DOFs) in the FEM model, is computationally expensive. To circumvent this problem several solution methods, such as modal superposition method [6], receptance based method [11–13] and structural modification techniques [14, 15] are developed. In addition, component mode synthesis (CMS) methods, which allow for the reduction of the original problem by several order of magnitude and are still accurate enough for the purpose of nonlinear dynamic analysis are also popular among the researchers; some example with friction contact problems are found in Refs. [8, 16–18]. These methods reduce the computation time while keeping the accuracy of the FEM model. Therefore, FEM representation is used in this thesis to accurately model the dynamics of the turbine bladed disk and the friction contact.

Another aspect that affects the prediction of the nonlinear forced response of the

system is the modelling of the contact interface that describes the essential interaction between the elastic bodies. These interactions can be geometrically divided in the normal and the tangential directions. A unilateral contact law is often considered in the normal direction and frictional law for the tangential contact, see Fig. 1.2. The most commonly used contact laws in the field of modelling of bladed disks are rigid and linear-elastic laws [19]. These contact laws clearly distinguish between stick and slip tangential motion and referred to as macroslip model. The elastic form of macroslip contact law is first introduced by Griffin [20] in this field and used by many researchers [7, 10, 21, 22]. The rigid form of macroslip contact law is described in Ref. [23] and also popular in the field [24–26]. Choice of the contact law depends on the solution method adopted in solving the equations of motion. Macroslip representation performs well in the small and moderate normal load cases, when gross-slip occurs at the friction interface. As oppose to macroslip model, microslip contact law does not distinguish between stick and slip tangential motion. Microslip is particularly important when normal contact load is high between the contacting bodies. The microslip model can be realized by macroslip contact law (elastic or rigid) using appropriate discretization of the contact interface or by using appropriate hysteresis law, such as Dahl [27], Iwan [28], LuGre and Valanis model [29]. In the field of friction damping of turbine bladed disks, microslip friction model with constant normal load is first studied by Menq et al. [30, 31] where the damper is modelled as an elastic beam with a shear layer and later by Csaba [4], where the shear layer is removed for simplicity. Microslip models for the complex contact kinematics, such as 1D and 2D tangential motion with variable normal load are developed by Cigeroglu [6, 32]. However, since the optimum friction damping is obtained in the gross-slip region [33, 34], macroslip models, due their mathematical simplicity, are widely used in the modelling of friction contacts, and therefore its elastic form is used in this thesis. Moreover, microslip effect is incorporated implicitly by discretizing the contact interface.

To compute the nonlinear contact forces, a mathematical description of the contact motion is required that is known as contact kinematics. Several contact models are developed in the literature [7, 21, 22, 35–37] for the simple contact kinematics (1D tangential motion and constant normal load) and complex contact kinematics (2D tangential motion and variable normal load). Computational methods of the nonlinear contact forces can be broadly classified as time-continuous (event-driven) and time-discrete scheme. In the time-continuous scheme, state (*stick*, *slip* and *separation*) transition times are resolved directly and an analytical expression is obtained between two states and this lead to a fast and accurate computation of the contact forces for the simple contact kinematics. However, often the state transition times are the roots of transcendental equations, that requires a numerical solution procedure [19] and this

makes time-continuous scheme comparatively expensive if numerous events occur per vibration period such as for a 3D contact kinematics. Furthermore, Gibbs phenomenon leads to artificial oscillations near discontinuities such as contact state transitions and gives rise to the number of events, those are not physical. This makes time-continuous scheme less attractive in the context of the frequency domain solution approach, where the contact forces are approximated as a truncated Fourier series, even though a time-continuous scheme gives an accurate description of the contact forces if transition times are resolved correctly. On the other hand, time-discrete scheme evaluates the nonlinear forces at discrete time steps and converts it into the frequency domain using fast Fourier transformation (FFT) and thus nonlinearity is easily handled by piecewise evaluation. This offers a greater flexibility in terms of the calculation of contact forces and its harmonics and different forms of contact laws can be easily integrated in this scheme. Moreover, an analytical expression is formulated in this thesis to compute the Jacobian matrix for full-3D friction contact model that efficiently evaluates the Jacobian matrix while computing the friction contact forces. This formulation reduces the computation time significantly and therefore time-discrete scheme is used here. Accuracy of the time-discrete scheme is limited by the number of points chosen in FFT scheme; however, the approach is more flexible compared to the time-continuous scheme, see PAPER-A.

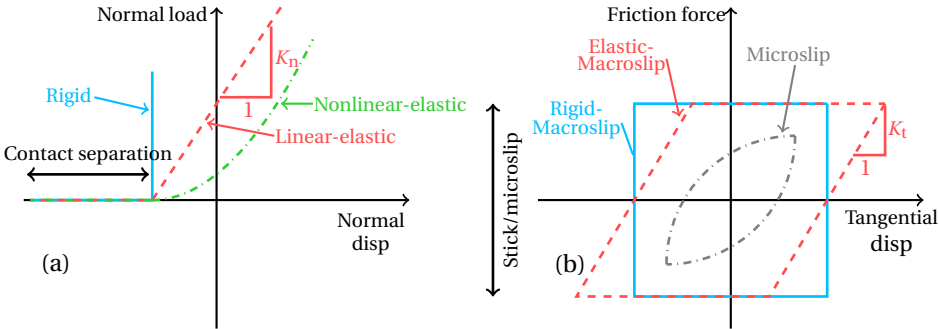


Figure 1.2: (a) Unilateral contact laws in the normal direction and (b) frictional contact laws in the tangential direction for 1D-harmonic displacement and constant normal load.

Finally, the frequency domain EQM results into a large set of nonlinear algebraic equations which need to be solved iteratively. This is a computationally expensive process if all the DOFs are kept inside the iteration loop. Therefore, several solution methods such as the structural modification technique, modal superposition method and receptance based approach are developed to circumvent the problem. Structural modification techniques are applied for the nonlinear analysis of bladed disk systems

in Refs. [14] and [15], where the nonlinear dynamic stiffness matrix is obtained by structural modification technique. This method is useful for few contact node problems and for simple contact kinematics, however it often fails to converge for complex contact kinematics where turning point bifurcations are observed, and therefore seldom applied for the analysis of complex structures. The modal superposition method developed in Ref. [6], reduces the number of DOFs to the number of mode shapes used in the formulation. This method is useful for multiple contact node problems such as for a mistuned assembly since the method is independent of the number of contact nodes. A disadvantage of this formulation is that the EQM is solved for the vector of modal harmonic coefficients, whereas, for the calculation of nonlinear contact forces the harmonic coefficients of the displacement vector are required. Therefore, at each iteration step, modal harmonic coefficients are converted into the displacement harmonics, which is a cost intensive process for few contact nodes. Unlike the modal superposition method, the receptance based method reduces the EQM to the nonlinear DOFs by using the dynamic compliance matrix (FRF) [11] and only keeps displacement harmonics of the contact DOFs inside the iteration loop and thus reduces the computational time significantly compare to all DOFs. Many variants for the computation FRF matrix such as CMS methods [8, 16–18] and high-accurate FRF method [38] are also well developed in the literature. These methods facilitate in accurate prediction of the FRF matrix by reducing the size of the problem and using few dynamic modes, respectively. Furthermore, accurate prediction of FRF is necessary to capture the local elasticity of the contact nodes at the interface. Therefore, receptance based method is preferred for macroslip modelling with few contact nodes and used by several researchers [12, 13, 39–41] as well as in this thesis.

1.2 The COMP project

The work presented in this thesis is performed within the COMP project, which is part of the TurboPower initiative [42]. The project is executed in close cooperation between Swedish gas turbine industry and several departments at KTH. The overall goal in the COMP is to develop and validate a computational tool to perform high cycle fatigue (HCF) predictions for components subjected to aero-dynamically induced vibrations. Important factors to be considered are the prediction accuracy and the computational speed.

The COMP project is divided into four work packages (WPs): WP1 Component mode synthesis (CMS) techniques, WP2 Aero-forcing and aero-damping, WP3 Structural damping and WP4 Material fatigue. The present work is performed within WP3 Structural damping.

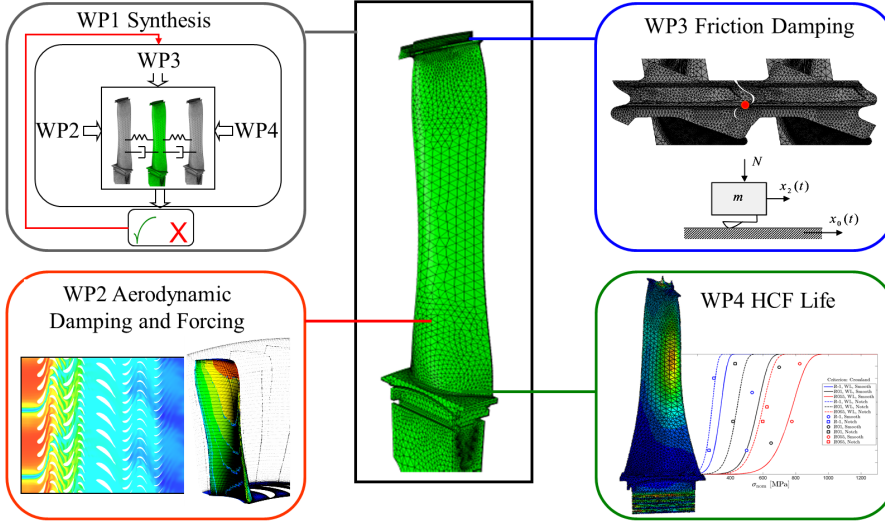


Figure 1.3: COMP project outline.

1.3 Objectives

The overall objective of this doctoral thesis is to develop a numerical simulation tool for parametric studies of friction damping on real turbine blades at the industrial level. The main contributions of the thesis can be summarized as follow

- The role of cyclic symmetry in reducing the number of DOFs in the linear and nonlinear analysis is studied and the cyclic symmetry boundary condition is implemented in the numerical simulation tool.
- A detail review of the friction contact models available in the literature is done and a full-3D time-discrete friction contact model is reformulated. Moreover, a method to compute the Jacobian matrix while computing the friction forces is derived and implemented in the simulation tool.
- While solving the nonlinear algebraic EQM, a method to control the step-length around the turning point bifurcation and on the steep branch of the curve is proposed to minimize the convergence problems.

- The developed numerical simulation tool is applied on a test case turbine blade and a real industrial bladed disk. Different types of friction contacts such as shroud contact, strip damper and multiple friction contacts are analyzed using the developed tool and obtained results are discussed.
- Finally, a proposal is made and a numerical investigation is performed to control the normal contact load at the friction interface of a bladed disk using magnetostrictive actuator.

The developed tool will be an integral part of the AROMA software, that is under development in the COMP project.

1.4 Organization of thesis

This thesis is organized as follows: Chapter 2 presents the concept of a cyclic structure and the role of cyclic symmetry properties in reducing the number of DOFs in the dynamic analysis. Chapter 3 discusses contact models available in the literature. Chapter 4 discusses the solution methods of the nonlinear algebraic equation and Chapter 5 presents an introduction of the magnetostrictive material Terfenol-D and its potential application in the field of friction damping of bladed disks. In Chapter 6 results for the test case blade and the real bladed disk are presented, in Chapter 7 the main conclusions and recommendations are given and finally, in Chapter 8 the appended papers are summarized.

CHAPTER 1. INTRODUCTION

2 Cyclic Structures

The structure of the mass and stiffness matrices for a cyclic structure are described in this chapter. The EQM of a full bladed disk is formulated in the time domain and subsequently reduced to a single sector by using the concept of the cyclic symmetry. Furthermore, the time domain displacements and forces are approximated as a Fourier series with multiple harmonics to convert the EQM in a set of nonlinear algebraic equations for cost effective iterative solution. This is known as multiharmonic balance method. The concept of travelling wave excitations and engine order excitations is also introduced.

2.1 Cyclic symmetric structures

Tuned bladed disks are cyclic symmetric structures. The mass and the stiffness matrices of cyclic structures have special characteristics that can be used to reduce the full bladed disk model to a single sector model. Therefore, the numerical effort in computing the system properties such as eigenvalues (natural frequencies) and eigenvectors (mode shapes) can be significantly reduced. Moreover, nonlinear contact forces on a single sector that depend on two adjacent sectors can also be computed using a single sector model (Fig. 1, PAPER-A).

$$\mathbf{M} = \begin{Bmatrix} \mathbf{M}_0 & \mathbf{M}_1 & \mathbf{0} & \dots & \mathbf{0} & \mathbf{M}_1^T \\ \mathbf{M}_1^T & \mathbf{M}_0 & \mathbf{M}_1 & \mathbf{0} & \dots & \mathbf{0} \\ \mathbf{0} & \mathbf{M}_1^T & \mathbf{M}_0 & \mathbf{M}_1 & \mathbf{0} & \dots \\ \vdots & \ddots & \ddots & \ddots & \ddots & \vdots \\ \mathbf{0} & \dots & \mathbf{0} & \mathbf{M}_1^T & \mathbf{M}_0 & \mathbf{M}_1 \\ \mathbf{M}_1 & \mathbf{0} & \dots & \mathbf{0} & \mathbf{M}_1^T & \mathbf{M}_0 \end{Bmatrix}. \quad (2.1)$$

Describing the mechanical properties in a cyclic coordinate system, the structure of the mass and the stiffness matrices of a tuned bladed disk displays a so-called block-

circulant form, for instance, shown in Eq. (2.1), for the mass matrix. The block-circulant mass and stiffness matrices are real and symmetric matrices of size $[n_b n_d \times n_b n_d]$, where n_b is the number of identical blades in the bladed disk and n_d is the number of degree of freedoms in a single sector. The symmetric submatrices \mathbf{M}_0 and \mathbf{M}_1 are of size $[n_d \times n_d]$. The submatrix \mathbf{M}_0 represents the interaction between the n_d degree of freedoms in each sector and the submatrix \mathbf{M}_1 describes the interaction between the degree of freedoms belonging to neighboring sectors of the cyclic symmetric structure.

2.2 Travelling wave excitation

Rotating bladed disks are excited by aerodynamic and other forces that travel relatively to the bladed disk due to the rotation of the bladed disk at a constant speed while preserving their spatial distribution [9]. In cylindrical coordinates fixed to the rotor, r , z , and φ , these forces can be expressed in the form: $\mathbf{f}_{\text{ext}}(r, z, \varphi \pm \Omega t)$, where the “-” sign corresponds to forward travelling wave and the “+” sign corresponds to backward travelling wave. The angular velocity of the bladed disk is Ω . All forces of this type satisfy the following relationship:

$$^{(k)}\mathbf{f}_{\text{s,ext}}(t) = {}^{(1)}\mathbf{f}_{\text{s,ext}}(t - (k-1)\Delta t), \quad (2.2)$$

where s stands for a single sector, t is the natural time and $k = 1, 2, \dots, n_b$. The time shift between two consecutive blades is $\Delta t = T/n_b$, where T is the period of one rotation.

For most turbomachinery applications, the excitation field exhibits a spatial periodicity, m , also referred to as “engine order”. Therefore, the time invariant excitation field in cylindrical coordinates fixed to the ground can be described by an infinite Fourier series

$$^{(k)}\mathbf{f}_{\text{s,ext}}(t) = \text{Re} \left\{ \sum_{n=0}^{\infty} {}^{(1)}\hat{\mathbf{f}}_{\text{s},n} e^{-inm(k-1)\phi} \right\}, \quad (2.3)$$

to find the excitation force on sector k , where ${}^{(1)}\hat{\mathbf{f}}_{\text{s},n}$ is the n th Fourier coefficient of the excitation force on the first sector. The inter blade phase angle (IBPA), $\phi = 2\pi/n_b$ is related to the time shift as $\Delta t = \phi/\Omega$ and the temporal periodicity is n . Transformation of the excitation forces into the cyclic rotating frame of reference fixed to the rotor results in

$$^{(k)}\mathbf{f}_{\text{s,ext}}(t) = \text{Re} \left\{ \sum_{n=0}^{\infty} {}^{(1)}\hat{\mathbf{f}}_{\text{s},n} e^{inm(\Omega t - (k-1)\phi)} \right\}. \quad (2.4)$$

Using Eq. (2.4), the excitation for the k th sector is derived from the excitation of the 1st sector. The excitation between two sectors only differs by the phase angle $m\phi$ which is

directly associated with the nodal diameter (ND) of the bladed disk, therefore it is also referred to as nodal excitation [9].

According to the nodal diameter map, known as ZZENF diagram [43], a nodal excitation can only excite the mode shape corresponding to a particular ND of the bladed disk, which depends both on the temporal periodicity n and the spatial periodicity m of the excitation. For example, an excitation with harmonic index $h = h(m, n) = \text{mod}(m \times n, n_b)$ can only excite the h th ND of the bladed disk in the backward travelling mode if $h \leq n_b/2$ and in the forward travelling mode of $(n_b - h)$ th ND if $h > n_b/2$, where n_b is an even number and mod is remainder operator. A detail explanation of the excited nodal diameter as a function of temporal harmonic n and the spatial harmonic m is found in Refs. [8, 39]. This leads to a reduction in the number of NDs and consequently, in the set of eigenvectors required to solve the equations of motion in the frequency domain.

2.3 The nonlinear equations of motion

2.3.1 Equations of motion of the full bladed disk

The EQM of a full bladed disk composed of n_b identical sectors with nonlinear contact at the shroud interface, is formulated in a cyclic frame of reference fixed to the bladed disk rotor as follows,

$$\mathbf{M}\ddot{\mathbf{q}}(t) + \mathbf{C}\dot{\mathbf{q}}(t) + \mathbf{K}\mathbf{q}(t) = \mathbf{f}_{\text{ext}}(t) - \mathbf{f}_{\text{nl}}(\mathbf{q}_{\text{nl}}(t), \dot{\mathbf{q}}_{\text{nl}}(t), t), \quad (2.5)$$

where \mathbf{M}, \mathbf{K} and \mathbf{C} are the conventional mass, stiffness and viscous damping matrices of the full bladed disk and $\mathbf{q}(t)$ represents the cyclic displacement vector. The vector $\mathbf{f}_{\text{ext}}(t)$ is the traveling wave excitation and $\mathbf{f}_{\text{nl}}(\mathbf{q}_{\text{nl}}(t), \dot{\mathbf{q}}_{\text{nl}}(t), t)$ represents the nonlinear contact force vector caused by friction and the relative displacement of the contact interface nodes. The displacements of the contact interface nodes are referred to as nonlinear displacements in this thesis and denoted as $\mathbf{q}_{\text{nl}}(t)$. The length of the displacement vector $\mathbf{q}(t)$ is $(n_b n_d \times 1)$ and assembled as,

$$\mathbf{q}(t) = [^{(1)}\mathbf{q}_s^T(t), \dots, ^{(k)}\mathbf{q}_s^T(t), \dots, ^{(n_d)}\mathbf{q}_s^T(t)], \quad (2.6)$$

where $^{(k)}\mathbf{q}_s(t)$ represents the displacement vector of the k th sector with $k = 1, 2, \dots, n_b$ and is of the size $(n_d \times 1)$. The structure of the nonlinear displacement vector $\mathbf{q}_{\text{nl}}(t)$, the excitation force $\mathbf{f}_{\text{ext}}(t)$ and the nonlinear interaction force $\mathbf{f}_{\text{nl}}(\mathbf{q}_{\text{nl}}(t), \dot{\mathbf{q}}_{\text{nl}}(t), t)$ is similar to the structure of the displacement vector in Eq. (2.6), only the size of the nonlinear displacement vector $\mathbf{q}_{\text{nl}}(t)$ is $(n_b n_{\text{nl}} \times 1)$, where n_{nl} is the number of nonlinear DOFs.

2.3.2 Equations of motion reduced to a single sector

Because of the travelling wave type excitation and the cyclic symmetry properties of bladed disk [8, 9], a relationship between the displacement vector of distinct sectors is defined similar to the relationship defined in Eq. (2.2) and reads

$$^{(k)}\mathbf{q}_s(t) = ^{(1)}\mathbf{q}_s(t - (k-1)\Delta t). \quad (2.7)$$

This is the fundamental relationship of the cyclic symmetric modelling, which allows for evaluation of the displacement vector for all sectors $^{(k)}\mathbf{q}_s(t)$ where $k = 2, 3, \dots, n_b$, using the first sector $^{(1)}\mathbf{q}_s(t)$ by applying a simple time shift shown in Eq. (2.7) [44].

To compute the nonlinear contact force $^{(k)}\mathbf{f}_{s,nl}(\mathbf{q}_{nl}(t))$ using a single sector, it is written as,

$$^{(k)}\mathbf{f}_{s,nl}(\mathbf{q}_{nl}(t)) = ^{(k)}\mathbf{f}_{s,nll}(\mathbf{q}_{nl}(t)) + ^{(k)}\mathbf{f}_{s,nlr}(\mathbf{q}_{nl}(t)), \quad (2.8)$$

where $^{(k)}\mathbf{f}_{s,nll}(\mathbf{q}_{nl}(t))$ and $^{(k)}\mathbf{f}_{s,nlr}(\mathbf{q}_{nl}(t))$ are the nonlinear contact force at the left and right interface of the k th sector, respectively. Time derivative of the nonlinear displacement is omitted in the above equation for brevity and in the following. The nonlinear contact force at the left and right interface are expressed as,

$$^{(k)}\mathbf{f}_{s,nll}(^{(k-1)}\mathbf{q}_{nl}(t), ^{(k)}\mathbf{q}_{nl}(t)) = ^{(k)}\mathbf{f}_{s,nll}(^{(k)}\mathbf{q}_{nl}(t + \Delta t), ^{(k)}\mathbf{q}_{nl}(t)) \quad (2.9)$$

and

$$^{(k)}\mathbf{f}_{s,nlr}(^{(k)}\mathbf{q}_{nl}(t), ^{(k+1)}\mathbf{q}_{nl}(t)) = ^{(k)}\mathbf{f}_{s,nlr}(^{(k)}\mathbf{q}_{nl}(t), ^{(k)}\mathbf{q}_{nl}(t - \Delta t)), \quad (2.10)$$

where cyclic symmetry property is used to relate the nonlinear DOFs at the $(k-1)$ th and $(k+1)$ th sectors to the nonlinear DOFs of the (k) th sector. Furthermore, following Newton's third law, the following relationship exists at the right interface of the (k) th and the left interface of the $(k+1)$ th sector (Fig. 1, PAPER-A),

$$^{(k)}\mathbf{f}_{s,nlr}(^{(k)}\mathbf{q}_{nl}(t), ^{(k+1)}\mathbf{q}_{nl}(t), t) = -^{(k+1)}\mathbf{f}_{s,nll}(^{(k)}\mathbf{q}_{nl}(t), ^{(k+1)}\mathbf{q}_{nl}(t), t). \quad (2.11)$$

Moreover, using the cyclic symmetry properties the following expression is obtained,

$$^{(k+1)}\mathbf{f}_{s,nll}(^{(k)}\mathbf{q}_{nl}(t), ^{(k+1)}\mathbf{q}_{nl}(t), t) = ^{(k)}\mathbf{f}_{s,nll}(^{(k-1)}\mathbf{q}_{nl}(t), ^{(k)}\mathbf{q}_{nl}(t), t - \Delta t), \quad (2.12)$$

and therefore using Eqs. (2.11)–(2.12), the following relationship between the right and left interface contact forces is derived,

$$^{(k)}\mathbf{f}_{s,nlr}(^{(k)}\mathbf{q}_{nl}(t), ^{(k+1)}\mathbf{q}_{nl}(t), t) = -^{(k)}\mathbf{f}_{s,nll}(^{(k-1)}\mathbf{q}_{nl}(t), ^{(k)}\mathbf{q}_{nl}(t), t - \Delta t). \quad (2.13)$$

Using the above equations, the nonlinear contact forces are computed using a single sector. Moreover, the nonlinear contact force at the right interface is derived from the

nonlinear contact force at the left interface and vice-versa. This reduces the computation time during the iterative solution of the EQM. Note that the above relationships are valid in the cyclic frame of reference.

Inserting the displacement vector (Eq. (2.6)) and the nonlinear contact force (Eq. (2.10)) into Eq. (2.5), and using the block-circulant form of the mass, stiffness and damping matrices results in

$$\begin{aligned}
 & \mathbf{M}_0^{(1)} \ddot{\mathbf{q}}_s(t_k) + \mathbf{M}_1^{(1)} \ddot{\mathbf{q}}_s(t_k - \Delta t) + \mathbf{M}_1^{T(1)} \ddot{\mathbf{q}}_s(t_k + \Delta t) + \mathbf{C}_0^{(1)} \dot{\mathbf{q}}_s(t_k) + \\
 & \mathbf{C}_1^{(1)} \dot{\mathbf{q}}_s(t_k - \Delta t) + \mathbf{C}_1^{T(1)} \dot{\mathbf{q}}_s(t_k + \Delta t) + \mathbf{K}_0^{(1)} \mathbf{q}_s(t_k) + \mathbf{K}_1^{(1)} \mathbf{q}_s(t_k - \Delta t) + \\
 & \mathbf{K}_1^{T(1)} \mathbf{q}_s(t_k + \Delta t) + {}^{(k)}\mathbf{f}_{s,nlr}({}^{(k)}\mathbf{q}_{nl}(t_k), {}^{(k)}\mathbf{q}_{nl}(t_k - \Delta t)) + \\
 & {}^{(k)}\mathbf{f}_{s,nll}({}^{(k)}\mathbf{q}_{nl}(t_k + \Delta t), {}^{(k)}\mathbf{q}_{nl}(t_k)) = {}^{(1)}\mathbf{f}_{s,ext}(t_k),
 \end{aligned} \tag{2.14}$$

for the (k) th sector, $k = 1, 2, \dots, n_b$, with $t_k = t - (k-1)\Delta t$. Note that the EQM of the (k) th sector in Eq. (2.14) only depend on the displacements of the first sector. Therefore, it is sufficient to consider the EQM of the first sector to evaluate the displacements of the full bladed disk for a tuned system [9, 44].

The EQM in Eq. (2.14) is a nonlinear delay differential equation. To solve Eq. (2.14), different approaches are used in the literature. The time domain simulation and the frequency domain simulation by using harmonic balance method (HBM) and multi-harmonic balance method (MHBm) are the most commonly used approach.

In the time domain approach, the nonlinear EQM are integrated numerically [4, 15, 21, 45] using a numerical integration technique, such as the finite difference method and the well known Runge-Kutta method. Time domain integration methods are easy to implement. However, steady state solutions are obtained through transient solutions and the nonlinear forces are evaluated at each time step that increases the computational time considerably. Due to the long computation times, time domain integration methods are rarely used for practical problems with many DOFs. However, time domain solutions are valuable in comparing the accuracy of other numerical methods. In some cases, to decrease the time spent in transient solutions steady state solution estimates, which are obtained by other solution methods, are used as initial conditions [4]. In general, to avoid the tedious and cost-intensive numerical integration of the EQM, the frequency domain method known as harmonic balance method (HBM) and describing function method [46] is extensively used in the forced response calculation of frictionally damped structure. In the HBM method, the displacement vector and nonlinear contact forces are approximated by a Fourier series truncated after the first harmonic. Approximating the nonlinear forces by the Fourier series, the nonlinear delay differential EQM (Eq. (2.14)) are converted to a set of nonlinear algebraic equations, which are then solved for the unknown harmonics. The HBM representation of the nonlinear forces has been used by many researchers [4, 12, 21, 36, 45];

however, a multiharmonic representation (MHBM) is preferred in recent publications [8–10, 16, 47] to capture the complex stick-slip motion of the damper more accurately. The MHBM increases the computation time by the number of harmonics used in the computation, therefore a trade-off is required between the number of harmonics used, computation time and computational accuracy. The MHBM representation is used in this thesis, and the formulation of the EQM in the frequency domain by using the Fourier–Galerkin's projection [48] is presented below.

2.3.3 Steady state solution by the multiharmonic balance method

To compute the periodic steady state response using the Fourier–Galerkin's method, the displacement vector $^{(1)}\mathbf{q}_s(t)$ of the first sector is approximated as a finite Fourier series truncated after n_h harmonics

$$^{(1)}\mathbf{q}_s(t) = \text{Re} \left\{ \sum_{n=0}^{n_h} {}^{(1)}\hat{\mathbf{q}}_{s,n} e^{inm\Omega t} \right\}, \quad (2.15)$$

where $^{(1)}\hat{\mathbf{q}}_{s,n}$ is the n th temporal harmonic coefficient of the displacement vector of length equal to the number of DOFs (n_d) in a single sector. Similar to $^{(1)}\mathbf{q}_s(t)$, time shifted displacement vectors $^{(1)}\mathbf{q}_s(t \pm \Delta t)$ are truncated as,

$$^{(1)}\mathbf{q}_s(t + \Delta t) = \text{Re} \left\{ \sum_{n=0}^{n_h} {}^{(1)}\hat{\mathbf{q}}_{s,n} e^{inm\Omega(t+\Delta t)} \right\} = \text{Re} \left\{ \sum_{n=0}^{n_h} {}^{(1)}\hat{\mathbf{q}}_{s,n} e^{inm\phi} e^{inm\Omega t} \right\} \quad (2.16)$$

and

$$^{(1)}\mathbf{q}_s(t - \Delta t) = \text{Re} \left\{ \sum_{n=0}^{n_h} {}^{(1)}\hat{\mathbf{q}}_{s,n} e^{inm\Omega(t-\Delta t)} \right\} = \text{Re} \left\{ \sum_{n=0}^{n_h} {}^{(1)}\hat{\mathbf{q}}_{s,n} e^{-inm\phi} e^{inm\Omega t} \right\}. \quad (2.17)$$

Furthermore, the nonlinear contact forces (Eq. (2.8)) truncated after n_h harmonics read as

$$^{(1)}\mathbf{f}_{s,nl}(\mathbf{q}_{nl}(t), t) = \text{Re} \left\{ \sum_{n=0}^{n_h} {}^{(1)}\hat{\mathbf{f}}_{nl,n} e^{inm\Omega t} \right\}. \quad (2.18)$$

Substituting Eqs. (2.15)–(2.18) and their derivatives into Eq. (2.14) and applying Galerkin's method results in a system of equations in the following form:

$$\hat{\mathbf{D}}(m, n, \Omega) \hat{\mathbf{q}}_{s,h} + \hat{\mathbf{f}}_{nl,h}(\hat{\mathbf{q}}_{nl,h}, m, n, \Omega) - \hat{\mathbf{f}}_{s,h} \approx \mathbf{0}. \quad (2.19)$$

From now on the left superscript (1) is omitted for brevity. Here, vector $\hat{\mathbf{q}}_{s,h}$ consists of the harmonics of all the DOFs (n_d) and $\hat{\mathbf{q}}_{nl,h}$ contains the harmonics of the nonlinear DOFs (n_{nl}) of a single sector. Since each DOF is described by $(n_h + 1)$ harmonics, $\hat{\mathbf{q}}_{s,h}$

and $\hat{\mathbf{q}}_{\text{nl},h}$ have length of $n_d(n_h + 1)$ and $n_{\text{nl}}(n_h + 1)$, respectively, and are assembled as

$$\hat{\mathbf{q}}_{\text{s},h} = \begin{bmatrix} \hat{\mathbf{q}}_{\text{s},0} \\ \hat{\mathbf{q}}_{\text{s},1} \\ \vdots \\ \hat{\mathbf{q}}_{\text{s},n_h} \end{bmatrix} \text{ and } \hat{\mathbf{q}}_{\text{nl},h} = \begin{bmatrix} \hat{\mathbf{q}}_{\text{nl},0} \\ \hat{\mathbf{q}}_{\text{nl},1} \\ \vdots \\ \hat{\mathbf{q}}_{\text{nl},n_h} \end{bmatrix}. \quad (2.20)$$

Similarly, external excitation forces and the nonlinear contact forces are assembled as

$$\hat{\mathbf{f}}_{\text{s},h} = \begin{bmatrix} \hat{\mathbf{f}}_{\text{s},0} \\ \hat{\mathbf{f}}_{\text{s},1} \\ \vdots \\ \hat{\mathbf{f}}_{\text{s},n_h} \end{bmatrix} \text{ and } \hat{\mathbf{f}}_{\text{nl},h} = \begin{bmatrix} \hat{\mathbf{f}}_{\text{nl},0} \\ \hat{\mathbf{f}}_{\text{nl},1} \\ \vdots \\ \hat{\mathbf{f}}_{\text{nl},n_h} \end{bmatrix}. \quad (2.21)$$

The dynamic stiffness matrix $\hat{\mathbf{D}}$ is a block-diagonal matrix and reads as

$$\hat{\mathbf{D}} = \text{blkdiag}(\hat{\mathbf{D}}_{0,\phi_m}, \hat{\mathbf{D}}_{1,\phi_m} \cdots \hat{\mathbf{D}}_{n_h,\phi_m}), \quad (2.22)$$

where each submatrix takes the form

$$\hat{\mathbf{D}}_n = \hat{\mathbf{K}}_{n,\phi_m} - (nm\Omega)^2 \hat{\mathbf{M}}_{n,\phi_m} + inm\Omega \hat{\mathbf{C}}_{n,\phi_m}, \quad (2.23)$$

for $n = 0, 1, \dots, n_h$, $\phi_m = m\phi$ and blkdiag represents the block diagonal operator. The mass, damping and stiffness matrices in $\hat{\mathbf{D}}_n$ are complex Hermitian matrices and related to block-circulant matrices as

$$\begin{aligned} \hat{\mathbf{M}}_{n,\delta_m} &= \mathbf{M}_0 + e^{-in\phi_m} \mathbf{M}_1 + e^{in\phi_m} \mathbf{M}_1^T, \\ \hat{\mathbf{K}}_{n,\delta_m} &= \mathbf{K}_0 + e^{-in\phi_m} \mathbf{K}_1 + e^{in\phi_m} \mathbf{K}_1^T \\ \text{and} \\ \hat{\mathbf{C}}_{n,\delta_m} &= \mathbf{C}_0 + e^{-in\phi_m} \mathbf{C}_1 + e^{in\phi_m} \mathbf{C}_1^T. \end{aligned} \quad (2.24)$$

These matrices are complex Hermitian and known as the structural matrices for the cyclic symmetric sector model. The matrices depend on both the temporal periodicity n and spatial periodicity m , and therefore each harmonic index $h = h(m, n) = \text{mod}(mn, n_b)$ has a different set of eigenvalues and eigenvectors, that should be considered while solving the EQM in the frequency domain. However, only a few harmonic indices are excited by the engine orders and nonlinear forces. This limits the number of sets of eigenvalues and eigenvectors required for the analysis. Furthermore, eigenvectors of a complex Hermitian matrix are complex and represented by rotating mode shapes instead of the standing waves. In this case, all eigenvectors are complex except for $h = 0$ and $h = n_b/2$. A further detail on this can be found in Refs. [39, 44].

Note that the submatrices $\mathbf{M}_0, \mathbf{K}_0$ and $\mathbf{M}_1, \mathbf{K}_1$ are part of each sector, therefore these matrices can be obtained using a single sector instead of using a full sector model by applying the complex cyclic constraints at the cyclic boundaries [9, 44].

Furthermore, the EQM in the frequency for a strip damper and multiple friction contacts are derived in PAPER-B and PAPER-C, respectively.

2.4 Conclusion

In this chapter, it is shown that by using cyclic symmetry properties, the nonlinear EQM of the full bladed disk with friction contact can be reduced to a single sector, which leads to a dramatic reduction in the number DOFs required in the EQM.

3 Contact Model

In this chapter, contact models developed in the literature are discussed. Time-discrete scheme that computes the nonlinear contact forces at discrete time steps as function of the relative displacement of the contact interface, contact interface parameters and normal load is introduced. Some simulation results for 1D and 2D tangential motion with constant and variable normal loads are presented and discussed. The effect of constant and variable contact stiffnesses are also analyzed. Finally, estimation methods of the contact stiffness values are discussed.

3.1 Background review

Friction damping in mechanical systems is obtained by the relative motion between vibrating bodies that induces stick-slip motion and therefore dissipates vibratory energy. The description of the relative motion between two surfaces in contact is known as contact kinematics, plays a key role in computing the contact forces and therefore in the resulted friction damping. Over the years, in the literature, several contact models have been developed. The main four contact models available are:

- 1D tangential relative displacement and constant normal load [20],
- 1D tangential relative displacement and variable normal load [7, 22],
- 2D tangential relative displacement and constant normal load [36, 49],
- 2D tangential displacement and variable normal load [45, 50].

The elastic form of macroslip contact model with 1D tangential motion and constant normal load is developed by Griffin [20] and further applied in Refs. [3, 51, 52] and others. This model is quite adequate for simple contact motion. However, as the contact kinematics become more complicated; for example, 2D elliptical relative motion

and motion with significant variation of the normal relative displacement, this contact model is not sophisticated enough to describe the contact motion. An illustration of the friction loop (hysteresis loop) for different contact kinematics is shown in Fig. 3.1, where K_t and K_n are the tangential and normal contact stiffness, respectively, and N_0 is the static component of the normal load. The friction coefficient is μ and X_A , Y_A and Z_A are the displacements in the tangential plane and in the normal direction, respectively. The phase difference between the displacements is ϕ and $\theta = m\Omega t$. The figure reveals that a change in the contact motion and the variation in the total normal load has a significant effect on the friction loop and hence on the amount of dissipated energy per oscillation. Therefore, an accurate, mathematically tractable and yet fast enough contact model is required to simulate complex structures like bladed disks.

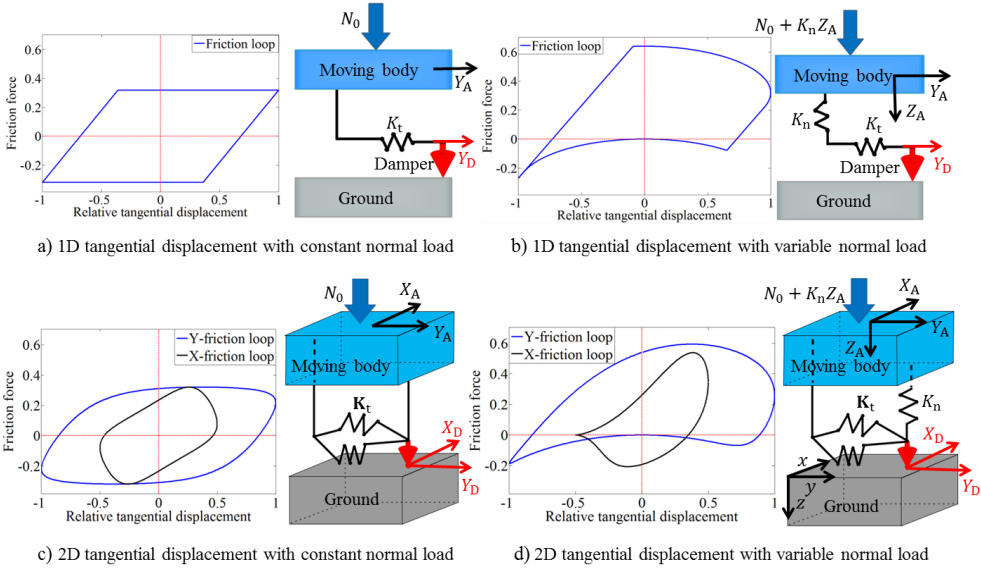


Figure 3.1: Input parameters for the friction loops are $K_t = K_n = 1\text{N/m}$, $N_0 = 0.8\text{N}$, $\mu = 0.4$, $X_A = 0.5\sin(\theta + \phi)\text{m}$, $Y_A = \sin(\theta)\text{m}$, $Z_A = 0.8\sin(\theta + \phi)\text{m}$, $\phi = \pi/2$, relative displacements and the friction forces are in meter and Newton, respectively.

Menq et al. [21] successfully develop an elastic macroslip contact model for 1D tangential motion with inphase variable load and later propose an approximate method to capture the 2D planar motion with constant normal load [53] using time-continuous approach. These models are fast and accurate but do not consider the general variation of normal load and full-3D contact kinematics. A more comprehensive friction contact model that considers normal load variation is developed by Yang et al. [22, 45, 49]. Petrov and Ewins [7] also formulate a time-continuous quasi-3D (two tangential directions are treated as uncoupled with variable normal load) friction contact elements

in the frequency domain with an analytical expression of the tangent stiffness matrix. Although evaluation of the contact forces using time-continuous scheme leads to accurate results, a change in the contact model requires a new evaluation of the contact forces and its harmonics, which limits the flexibility of the contact model [39]. Moreover, 3D time-continuous contact models are rarely used in industrial applications due to the large computational costs [54].

Alternate to the time-continuous method, the time-discrete approach has been used by many researchers in computing the nonlinear contact forces [8, 10, 37, 50]. In this approach, harmonics of the relative displacement (initial guess), recall MHBM chapter 2, are first converted to the time domain displacement at the sought frequency. Then the nonlinear contact forces are directly computed in the time domain that allows capturing complex nonlinearities exhibited by the friction forces and the normal load. Furthermore, different types of contact models including microslip model and measured hysteresis loop can be easily implemented in this scheme while keeping the computational advantage of the frequency domain modeling. Finally, these time domain nonlinear contact forces are transformed back to the frequency domain by means of the FFT algorithm for the computation of the final relative displacement by solving the nonlinear algebraic equations. This hybrid frequency-time domain approach is proposed by Cameron and Griffin [55] and known as alternate frequency time domain method (AFT), see Fig. 5 PAPER-A.

To compute the nonlinear friction forces in the time domain, Sanliturk [36] develops a time-discrete contact model for 2D tangential motion with constant normal load, as an extension of Menq et al. [53]. The algorithm is not only restricted to the Coulomb friction law. It can compute the friction forces based on theoretical models and on measured friction loop. The algorithm constitutes a basis for the further development of 3D time-discrete friction contact models as presented by Shi yajie and Gu et al. [37, 40, 50]. In PAPER-A of this thesis, a full-3D time-discrete friction contact model is reformulated and moreover an analytical expression for the Jacobian matrix is derived. It reduces the computation time significantly in the Newton–Raphson method that is used to solve the nonlinear algebraic EQM. Details of the contact model can be found in PAPER-A.

3.2 Simulation results

To demonstrate the flexibility of the time-discrete contact model, few examples are presented below. A linear-elastic contact law is used in the normal direction and elastic Coulomb law is employed in the tangential plane. The static component of the normal load is N_0 and the variable component of the normal is defined as $K_n Z_A$. The obtained

friction loops for multiharmonic input displacements, considering constant and variable contact stiffnesses are drawn in Figs. 3.2 and 3.3, respectively, for the case of 1D tangential motion and variable normal load.

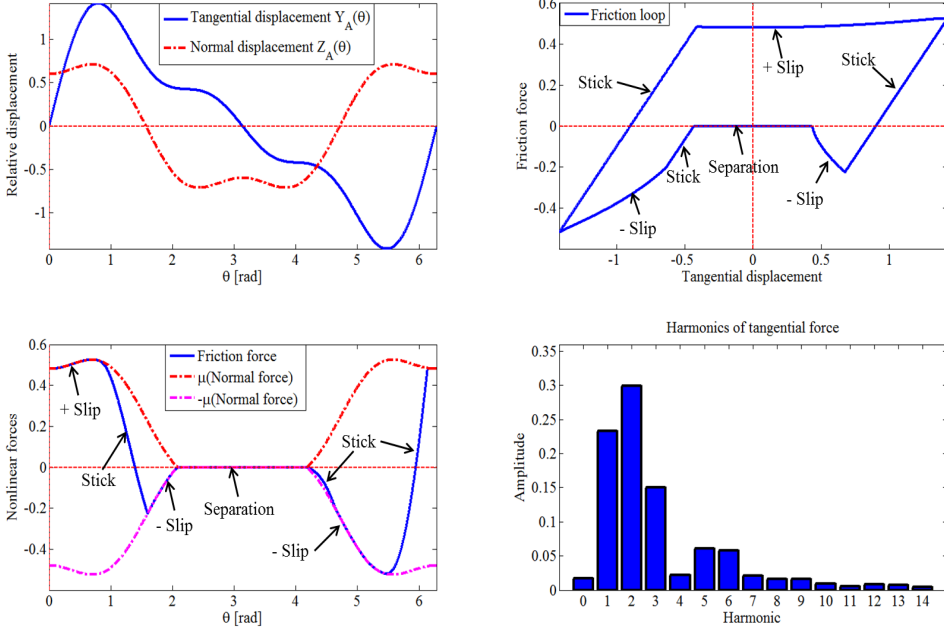


Figure 3.2: Friction loop for 1D tangential motion and variable normal load with constant contact stiffness values. Input parameters are $K_t = K_n = 1\text{N/m}$, $N_0 = 0.6\text{N}$, $\mu = 0.4$, $Y_A = \sin(\theta) + 0.5\sin(2\theta) + 0.3\sin(3\theta)\text{m}$, $Z_A = 0.8\sin(\theta + \phi) + 0.2\sin(3(\theta + \phi))\text{m}$, $\phi = \pi/2$, relative displacements and the friction forces are in meter and Newton, respectively.

The input tangential and normal displacements are shown in the top-left of the figures. In Fig. 3.2, the input motions include the first three harmonics, whereas, in the resulting friction force, six harmonics have significant contributions. This is due to the associated nonlinearity with complex stick-slip tangential motion and elastic normal contact law, which advocates considering the higher harmonics in the formulation of the EQM, even for input displacements are mono-harmonic. Furthermore, the friction loop is more complicated for the case of variable contact stiffnesses, see Fig. 3.3. Variable contact stiffness is required in the case of non-planar contact interfaces (e.g. contact interface of a sphere and a cylinder with a planar surface), according to the Hertz contact theory [56] and Mindlin's theory [57]. Variation of the contact stiffness values in the field of friction damping is verified in Refs. [58–61]. Note that these friction loops are drawn using a 3D time-discrete friction contact model by substituting $X_A = 0$ and changing the input parameters in the time domain accordingly.

3.2. SIMULATION RESULTS

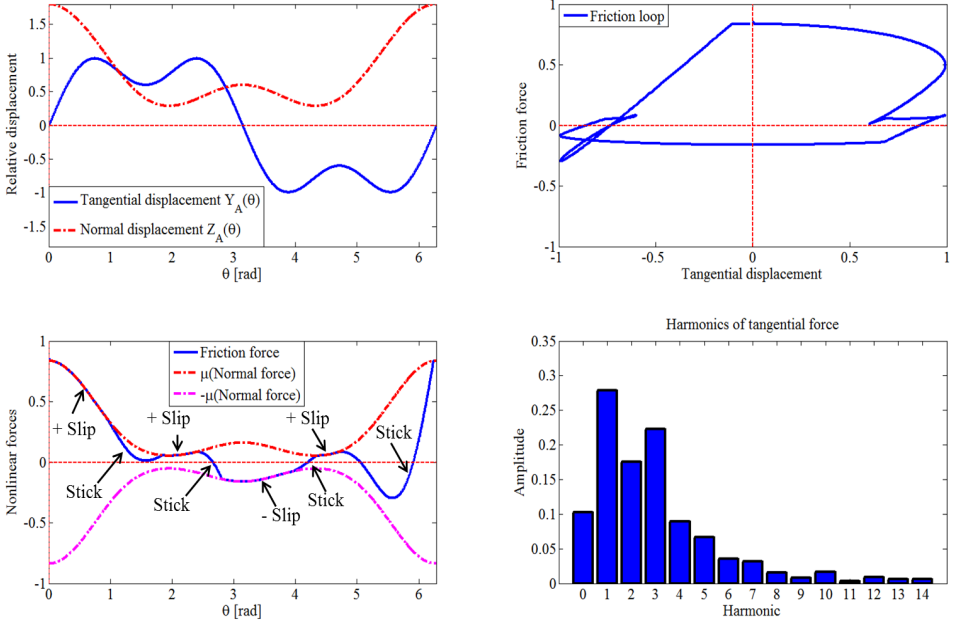


Figure 3.3: Friction loop for 1D tangential motion and variable normal load with variable contact stiffness values. Input parameters are $K_t = \sqrt{Z_A} \text{ N/m}$, $K_n = \sqrt{3Z_A}/2 \text{ N/m}$, $N_0 = 0 \text{ N}$, $\mu = 0.4$, $Y_A = \sin(\theta) + 0.4\sin(3\theta) \text{ m}$, $Z_A = 0.8 + 0.6\sin(\theta + \phi) + 0.4\sin(2\theta + \phi) \text{ m}$, $\phi = \pi/2$, relative displacements and the friction forces are in meter and Newton, respectively.

A similar analysis is performed for 2D tangential motion with variable normal load. In Fig. 3.4, the obtained friction loop for the constant contact stiffness and multiharmonic input displacement is drawn. Here again, six harmonics are found in the nonlinear contact force, whereas the displacement contains only three harmonics. Note that in the case of 2D planar motion, negative and positive slip boundary of the 1D tangential motion is replaced by “slip loop”. The slip loop is the limiting friction force curve for 2D planar motion that is used to identify the state (*stick*, *slip* or *separation*) of the friction contact as shown in the figure (bottom-left). The friction loop for the variable contact stiffnesses is plotted in Fig. 3.5. A variable contact stiffness changes the shape of the friction loop and the slip loop significantly, however both the friction loops are complex in nature and author believes that a time-continuous approach will consume a larger computation time in resolving the state transition times in these cases compared to the time-discrete approach applied here. Therefore, the time-discrete method should be preferred in the case of complex contact kinematics.

CHAPTER 3. CONTACT MODEL

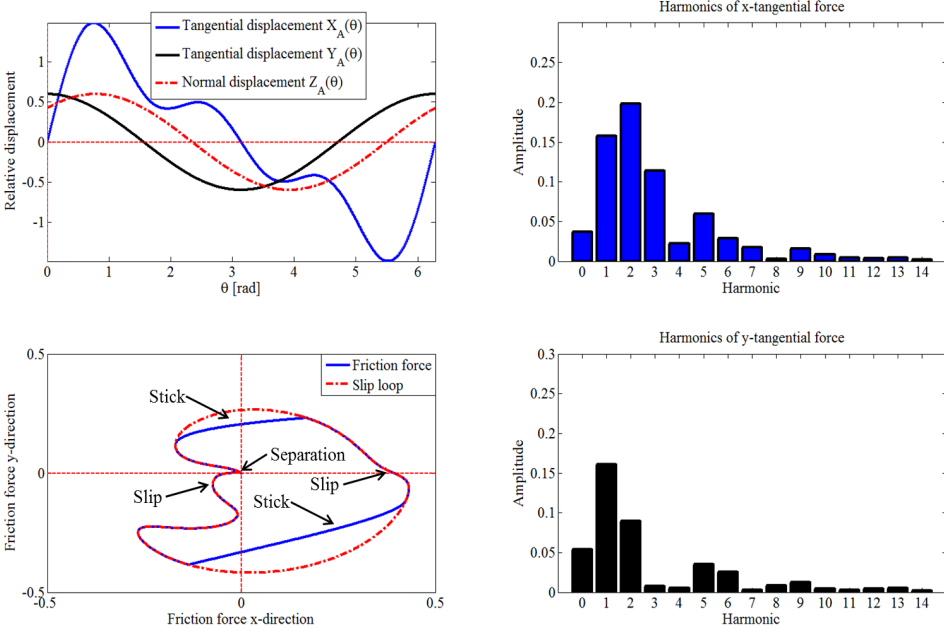


Figure 3.4: Friction loop for 2D tangential motion and variable normal load with constant contact stiffness values. Input parameters are $K_t = K_n = 1\text{N/m}$, $N_0 = 0.5\text{N}$, $\mu = 0.4$, $X_A = \sin(\theta) + 0.5\sin(2\theta) + 0.4\sin(3\theta)\text{ m}$, $Y_A = 0.6\cos(\theta)\text{ m}$, $Z_A = 0.6\sin(\theta + \phi)\text{ m}$, $\phi = \pi/4$, relative displacements and the friction forces are in meter and Newton, respectively.

Finally, to analyze the difference between constant and variable contact stiffness, a comparison curve is drawn for the same input motions (Fig. 3.6). Input parameters are:

$$\begin{aligned} X_A &= \sin(\theta) + 0.5\sin(2\theta) + 0.4\sin(3\theta)\text{ m}, \\ Y_A &= 0.6\cos(\theta)\text{ m}, \\ Z_A &= 0.4 + 0.6\sin(\theta + \phi)\text{ m}, \phi = \pi/4, \end{aligned} \quad (3.1)$$

and the contact stiffnesses are,

$$\mathbf{K}_t = \begin{bmatrix} 1 & 0 \\ 0 & 1 \end{bmatrix} \begin{cases} \sqrt{Z_A}\text{N/m}, & \text{if } Z_A \geq 0 \\ 0\text{N/m}, & \text{otherwise} \end{cases} \quad (3.2)$$

and

$$K_n = \begin{cases} \frac{\sqrt{3Z_A}}{2}\text{N/m}, & \text{if } Z_A \geq 0 \\ 0\text{N/m}, & \text{otherwise.} \end{cases} \quad (3.3)$$

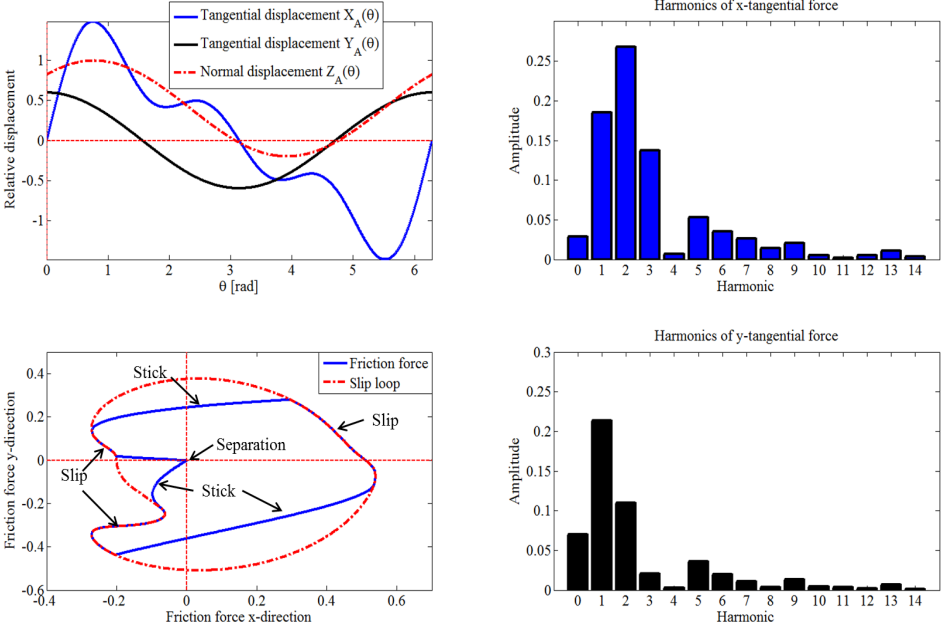


Figure 3.5: Friction loop for 1D tangential motion and variable normal load with variable contact stiffness values. Input parameters are $K_t = \sqrt{Z_A}N/m$, $K_n = \sqrt{3Z_A}/2N/m$, $N_0 = 0.5N$, $\mu = 0.4$, $X_A = \sin(\theta) + 0.5\sin(2\theta) + 0.4\sin(3\theta)$ m, $Y_A = 0.6\cos(\theta)$ m, $Z_A = 0.4 + 0.6\sin(\theta + \phi)$ m, $\phi = \pi/4$, relative displacements and the friction forces are in meter and Newton, respectively.

Mean stiffness values of the variable contact stiffness are used as constant stiffness. A significant difference is observed in both the curves, with the loop area for the variable contact stiffness is approximately 1.5 times of the constant contact stiffness case. Furthermore, the friction loop with variable contact stiffness passes through (0,0), this means separation occurs during a periodic cycle, whereas no separation is observed in the constant stiffness loop. These differences can have a profound effect on the forced response of the bladed disk.

3.3 Conclusion

Friction loops are drawn for single and multiharmonic input motions. Higher harmonics of the contact forces are observed even for a single harmonic input displacement, which shows that the multiharmonic formulation of the EQM is needed for nonlinear friction contact analysis. Friction loops are also drawn for constant and variable contact stiffnesses and a significant difference in the loop area is observed. This shows that interface parameters (K_t and K_n) can have a profound effect on the forced response of

the bladed disk. Finally, the estimation methods of the contact stiffness values are outlined.

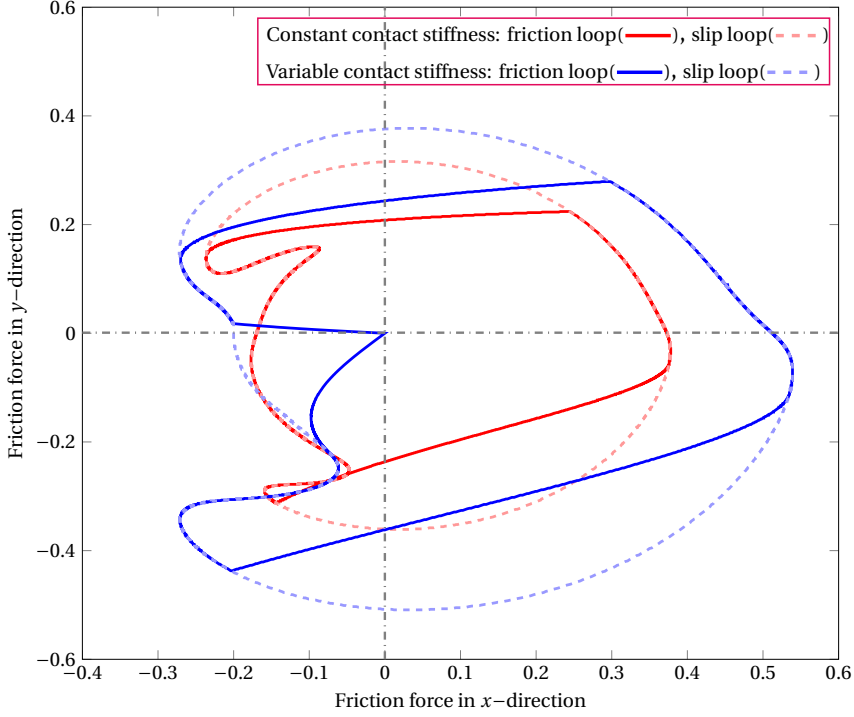


Figure 3.6: Comparison of constant and variable contact stiffness friction loop.

4 Solution of Nonlinear Algebraic Equations

In chapter 2, the EQM of a tuned bladed disk is reduced to a single sector by using the concept of cyclic symmetry. However, for a complex structure, a single sector still consists of thousand DOFs that is impossible to handle in an iterative solution. Therefore, in this chapter, the nonlinear EQM is further reduced to the contact DOFs only by using the receptance based approach. Furthermore, complex contact kinematics (tangential motion with variable normal loads) are prone to separation at low normal loads and in the case of an initial gap between the contact interfaces, what leads to turning point bifurcation in the nonlinear forced response curve. Solution methods for these cases are discussed here since the standard Newton–Raphson method fails at the turning points. Moreover, a method to control the step length during the iterative solution is also proposed.

4.1 Receptance based method

Finite element models are often used in the forced response analysis of complex structures with many DOFs. Due to the friction contact, this results in large systems of nonlinear equations which need to be solved iteratively. This is a computationally expensive and also an inefficient process if all the DOFs are kept inside the iteration loop. Menq and Griffin [11] develop a nonlinear forced response analysis method for the steady state response of frictionally damped structures using finite element models. In this method, DOFs are divided into linear and nonlinear DOFs (DOFs correspond to the nonlinear contact interface), and nonlinear equations are reduced to the number of nonlinear DOFs in the system, which is often a fraction of the total number of DOFs. This method is also known as receptance based method and used by several researchers [12, 13, 39–41] and in this thesis. Applying the receptance based approach, the EQM

in Eq. (2.19) can be rewritten as:

$$\begin{bmatrix} \hat{\mathbf{q}}_{\text{lin},h} \\ \hat{\mathbf{q}}_{\text{nl},h} \end{bmatrix} = \begin{bmatrix} \hat{\mathbf{R}}_{\text{lin},\text{lin}}(m, n, \Omega) & \hat{\mathbf{R}}_{\text{lin},\text{nl}}(m, n, \Omega) \\ \hat{\mathbf{R}}_{\text{nl},\text{lin}}(m, n, \Omega) & \hat{\mathbf{R}}_{\text{nl},\text{nl}}(m, n, \Omega) \end{bmatrix} \left\{ \begin{bmatrix} \hat{\mathbf{f}}_{\text{lin},s} \\ \hat{\mathbf{f}}_{\text{nl},s} \end{bmatrix} - \begin{bmatrix} \mathbf{0} \\ \hat{\mathbf{f}}_{\text{nl},h}(\hat{\mathbf{q}}_{\text{nl},h}, m, n, \Omega) \end{bmatrix} \right\}, \quad (4.1)$$

leading to

$$\hat{\mathbf{q}}_{\text{nl},h} - \hat{\mathbf{q}}_{\text{nl},h0} + \hat{\mathbf{R}}_{\text{nl},\text{nl}}(m, n, \Omega) \hat{\mathbf{f}}_{\text{nl},h}(\hat{\mathbf{q}}_{\text{nl},h}, m, n, \Omega) = 0, \quad (4.2)$$

where $\hat{\mathbf{q}}_{\text{nl},h0} = \hat{\mathbf{R}}_{\text{lin},\text{lin}}(m, n, \Omega) \hat{\mathbf{f}}_{\text{lin},s} + \hat{\mathbf{R}}_{\text{nl},\text{nl}}(m, n, \Omega) \hat{\mathbf{f}}_{\text{nl},s}$ represents the linear response of the nonlinear DOFs in the absence of the friction contact. The matrix $\hat{\mathbf{R}}_{\text{nl},\text{nl}}(m, n, \Omega)$ is known as the dynamic compliance matrix (FRF matrix), which is the inverse of the dynamic stiffness matrix $\hat{\mathbf{D}}_{\text{nl},\text{nl}}$, that is a part of the full dynamic stiffness matrix $\hat{\mathbf{D}}(m, n, \Omega)$, see Eq. (2.19). Once the steady state response of the nonlinear DOFs are computed, the steady response of linear DOFs are obtained as

$$\hat{\mathbf{q}}_{\text{lin},h} = \hat{\mathbf{q}}_{\text{lin},h0} - \hat{\mathbf{R}}_{\text{lin},\text{nl}}(m, n, \Omega) \hat{\mathbf{f}}_{\text{nl},h}(\hat{\mathbf{q}}_{\text{nl},h}, m, n, \Omega), \quad (4.3)$$

where $\hat{\mathbf{q}}_{\text{lin},h0}$ is the response of the linear DOFs in the absence of the friction contact.

Often, the Newton–Raphson method is applied to solve the reduced Eq. (4.2). An iterative step for Eq. (4.2) is expressed as

$$\hat{\mathbf{q}}_{\text{nl},h}^{(p+1)} = \hat{\mathbf{q}}_{\text{nl},h}^{(p)} - \left\{ \frac{\partial \mathbf{e}(\hat{\mathbf{q}}_{\text{nl},h}^{(p)})}{\partial \hat{\mathbf{q}}_{\text{nl},h}^{(p)}} \right\}^{-1} \mathbf{e}(\hat{\mathbf{q}}_{\text{nl},h}^{(p)}), \quad (4.4)$$

where $\hat{\mathbf{q}}_{\text{nl},h}^{(p)}$ and $\mathbf{e}(\hat{\mathbf{q}}_{\text{nl},h}^{(p)})$ are the nonlinear displacement vector and the residual vector at the p th iteration step, respectively. The residual vector and the Jacobian matrix at the p th step is defined as,

$$\begin{aligned} \mathbf{e}(\hat{\mathbf{q}}_{\text{nl},h}^{(p)}) &= \hat{\mathbf{q}}_{\text{nl},h}^{(p)} - \hat{\mathbf{q}}_{\text{nl},h0} + \hat{\mathbf{R}}_{\text{nl},\text{nl}}(m, n, \Omega) \hat{\mathbf{f}}_{\text{nl},h}^{(p)}(\hat{\mathbf{q}}_{\text{nl},h}^{(p)}, m, n, \Omega) \text{ and} \\ \mathbf{J}^{(p)} &= \left\{ \frac{\partial \mathbf{e}(\hat{\mathbf{q}}_{\text{nl},h}^{(p)})}{\partial \hat{\mathbf{q}}_{\text{nl},h}^{(p)}} \right\}. \end{aligned} \quad (4.5)$$

The nonlinear algebraic Eq. (4.2) often reveals turning point bifurcations [62] caused by the variation of normal load, especially in the case of the gap nonlinearities. In such cases, the standard Newton iteration step defined in Eq. (4.4) fails to converge around the turning point, where the Jacobian matrix is close to singular. To circumvent this drawback, a predictor-corrector continuation method is applied and therefore the system of equations is augmented with an additional constraint equation. There are many possibilities for the additional constraint equations; two of them are summarized below:

(a) A solution is sought on a hyperplane (linear constraint) orthogonal to the tangent vector at the previous converged point, see Fig. 4.1. Therefore, the system of equations for the computation of the response curve reads as,

$$\begin{aligned} \mathbf{e}(\mathbf{q}, \omega) &= \mathbf{0}, \\ \mathbf{v}_{\mathbf{q}}^T (\mathbf{q} - \mathbf{q}_{i+1}^{(1)}) + \nu_{\omega} (\omega - \omega_{i+1}^{(1)}) &= 0. \end{aligned} \quad (4.6)$$

This is known as Keller's method [63]. Here, $\mathbf{v} = \{\mathbf{v}_{\mathbf{q}}^T, \nu_{\omega}\}^T$ is the tangent vector and $(\mathbf{q}_{i+1}^{(1)}, \omega_{i+1}^{(1)})$ is the initial guess computed at predictor step, see Sec. 4.2. Note that $\omega = n\Omega$ is a variable in the continuation method, since the solution is searched along a hyperplane, not at the fixed frequency step.

(b) A solution is sought along the spherical constraint and therefore, the system of equations reads as,

$$\begin{aligned} \mathbf{e}(\mathbf{q}, \omega) &= \mathbf{0}, \\ \|\Delta \mathbf{q}, \Delta \omega\| &= \Delta s. \end{aligned} \quad (4.7)$$

This is known as Crisfield's method [64]. Here, $\Delta \mathbf{q} = (\mathbf{q}_{i+1}^{(1)} - \mathbf{q}_i)$, $\Delta \omega = (\omega_{i+1}^{(1)} - \omega_i)$ and (\mathbf{q}_i, ω_i) is the converged solution at the i th solution step. $\|\cdot\|$ represents the l_2 norm and Δs is step-length, the radius of the spherical constraint. Due to the presence of quadratic constraint equation in the Crisfield's method, solving Eq. (4.7) is rather cumbersome; therefore Keller's method is applied in this thesis.

A predictor-corrector continuation method generally consists of the following steps that will be discussed below:

- Predictor step,
- Corrector step,
- Step length control.

4.2 Predictor step

The first solution point in the continuation method is obtained using the standard Newton–Raphson method, where the first converged solution (\mathbf{q}_1, ω_1) is obtained from the initial guess of the linear solution. However, the initial guess $(\mathbf{q}_{i+1}^{(1)}, \omega_{i+1}^{(1)})$ at the $(i+1)$ th, $i = 1, 2, 3, \dots$ solution step is sought along the tangent vector at the previous converged solution (\mathbf{q}_i, ω_i) , known as predictor step, see Fig. 4.1. Once the tangent

vector \mathbf{v}_i at the i th converged solution is known, by applying a forward Euler scheme, the initial guess for the $(i + 1)$ th solution step is evaluated as,

$$\begin{bmatrix} \mathbf{q}_{i+1}^{(1)} \\ \omega_{i+1}^{(1)} \end{bmatrix} = \begin{bmatrix} \mathbf{q}_i \\ \omega_i \end{bmatrix} + \Delta s_i \frac{\mathbf{v}_i}{\|\mathbf{v}_i\|}. \quad (4.8)$$

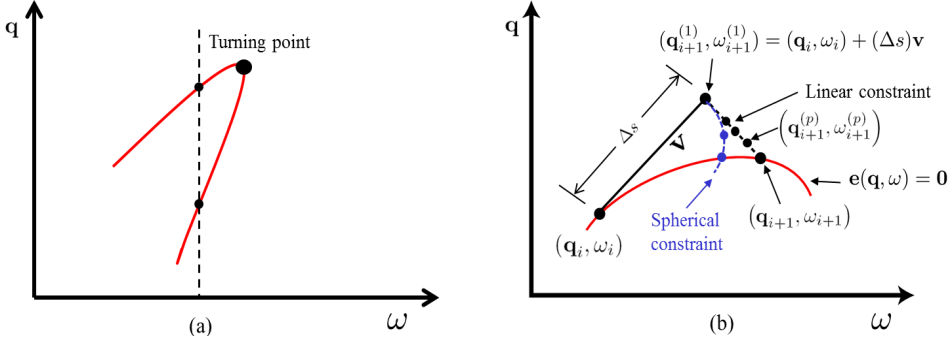


Figure 4.1: Turning point bifurcation [Paper-A].

Let $\mathbf{A} = \begin{bmatrix} \mathbf{e}_{\mathbf{q}} & \mathbf{e}_{\omega} \end{bmatrix}$, where $\mathbf{e}_{\mathbf{q}} = \mathbf{J} = \left\{ \frac{\partial \mathbf{e}(\mathbf{q}, \omega)}{\partial \mathbf{q}} \right\}$ and $\mathbf{e}_{\omega} = \left\{ \frac{\partial \mathbf{e}(\mathbf{q}, \omega)}{\partial \omega} \right\}$. The tangent vector at the first converged solution (\mathbf{q}_1, ω_1) is obtained by the **QR** decomposition of \mathbf{A}^T and represented by the last column of the matrix \mathbf{Q} [65]. Further, it is normalized such that $\|\mathbf{v}_1\| = 1$. The tangent vector at the first converged solution is also obtained as,

$$v_{\omega,1} = \pm 1 / \|\mathbf{l}, \mathbf{w}\|, \quad \mathbf{v}_{\mathbf{q},1} = -v_{\omega,1} \mathbf{w}, \quad (4.9)$$

where $\mathbf{w} = \{\mathbf{e}_{\mathbf{q}}^{(-1)} \times \mathbf{e}_{\omega}\}_{(\mathbf{q}_1, \omega_1)}$. Note that the Eq. (4.9) has two possible solutions for $v_{\omega,1}$: $v_{\omega,1} > 0$ should be used for the upward sweeping and, $v_{\omega,1} < 0$ for downward sweeping. Subsequently, direction vectors are obtained by solving,

$$\begin{bmatrix} \mathbf{A}_i \\ \mathbf{v}_{i-1}^T \end{bmatrix} \begin{bmatrix} \mathbf{v}_i \\ 1 \end{bmatrix} = \begin{bmatrix} \mathbf{0} \\ 1 \end{bmatrix}. \quad (4.10)$$

The equation $\mathbf{v}_{i-1}^T \mathbf{v}_i = 1$, is used to preserve the direction of the tangent vector. The tangent vector is also obtained by normalizing,

$$\mathbf{v}_i = \frac{\begin{bmatrix} \mathbf{q}_i \\ \omega_i \end{bmatrix} - \begin{bmatrix} \mathbf{q}_{i-1} \\ \omega_{i-1} \end{bmatrix}}{\Delta s_{i-1}}. \quad (4.11)$$

4.3 Corrector step

Generally, we will get a nonzero residue after the predictor step (unless the problem is linear), i.e. $\mathbf{e}(\mathbf{q}_{i+1}^{(1)}, \omega_{i+1}^{(1)}) \neq 0$. To return to the equilibrium path, an iterative scheme is required starting from this point. Therefore, the purpose of the correction step is to iteratively obtain a better approximation of the next point until some predefined tolerances are met. Pseudo-arclength continuation is used here, in which the Newton iteration step is applied on the extended system of equations, Eq. (4.6). Therefore, the next approximation is obtained as,

$$\begin{bmatrix} \mathbf{q}_{i+1}^{(p+1)} \\ \omega_{i+1}^{(p+1)} \end{bmatrix} = \begin{bmatrix} \mathbf{q}_{i+1}^{(p)} \\ \omega_{i+1}^{(p)} \end{bmatrix} - \begin{bmatrix} \mathbf{A}_i \\ \mathbf{v}_i^T \end{bmatrix}^{-1} \begin{bmatrix} \mathbf{e}(\mathbf{q}_{i+1}^{(p)}, \omega_{i+1}^{(p)}) \\ 0 \end{bmatrix}. \quad (4.12)$$

Note that the Jacobian matrix of the pseudo-arclength continuation, Eq. (4.12) is non-singular at the turning point. This corrector step is repeated until convergence is obtained or the predefined maximum iteration step is reached.

4.4 Step length control

Step-length control is an important part of a continuation method. If the step-length is too small, then a lot of unnecessary work is done. If it is too large, then the corrector algorithm may converge to a point on a different branch or not converge at all, see Fig. 4.2(b). Therefore, a good estimate of step-length and adaptation method is required in order to optimize the computation time while tracing the response curve accurately. There are many ways to introduce the step-length adaption. These are mainly based on the performance of the Newton iterations. For example, a simple scheme may be that we increase the step-length whenever few Newton iterations were needed to compute the last point, and conversely, we decrease the step-length when the previous point needed many Newton iterations. Therefore at each step, the value of the step-length is adapted according to,

$$\Delta s_i = \Delta s_{(i-1)} \sqrt{\frac{N_{\text{iter}}^*}{N_{\text{iter}}^i}}, \quad (4.13)$$

where N_{iter}^i is the number of iterations required for convergence at i th solution step and N_{iter}^* is the user chosen threshold number of iterations. The N_{iter}^* indirectly controls the actual step-length used in computations. Usually, this value is set to three or four iterations per step to trace the nonlinear dynamic path. Few more control strategies can be found in [62]. However, all these methods are based either on the

number of iterations and on the tolerance value at each iteration step. It does not take particular care of the turning point and therefore, the iteration steps often fail to converge due to the large step-length or converge to a different branch, see Fig. 4.2(b).

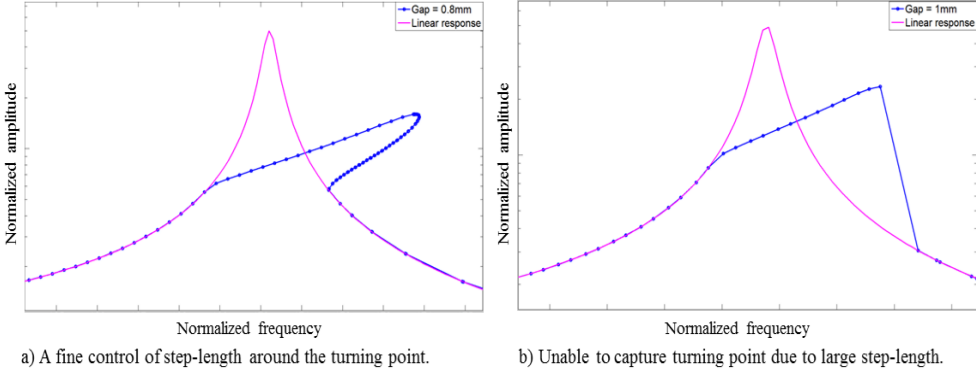


Figure 4.2: Effect of fine control of step-length on the response curve.

In this thesis, in addition to the above adaptation, a method is proposed that facilitates a fine control of the step-length around the turning point based on the direction vector, v_ω . It should be noted that sign of v_ω changes around the turning point from positive to negative and vice versa, therefore as the continuation algorithm encounters $v_{\omega,(i-1)} * v_{\omega,(i)} < 0$, it moves back the solution by two or three step and recalculate the solution with a step-length of 1/10th of the currently in used. The effect of the new strategy to control the step-length around the turning point can be seen in Fig. 4.2(a). Moreover, an additional control strategy for the steep branch of the curve has also been implemented in the code, that is determined by the norm of \mathbf{v}_q and formulated as,

$$\|v_{q,i}\| > \alpha \|v_{q,i-1}\|, \quad (4.14)$$

where α has a constant value ranging 20 – 40. If the above criteria are satisfied then the maximum step-length is restricted for those solution points. This helps in controlling the convergence failure around the resonance and the steep portion of the curve.

Implementing the above control strategy, a smaller step-length size is used around the turning point and on the steep branch of the curve to avoid convergence failure and branch switching, while on the other portion of the curve large step-length is employed. Therefore, it optimizes the computation time while tracing the accurate dynamic behavior.

4.5 Conclusion

The EQM of a single sector is reduced to the nonlinear DOFs using the receptance based method and the solution methods (continuation methods) for nonlinear algebraic equations with turning point bifurcation are discussed. A method is proposed to control the step-length at the turning points and on the steep branch of the curve, which play an important role in the convergence of continuation methods.

5 Magnetostrictive Materials

Historical overview and physics of magnetostrictive materials are presented in this chapter. The most famous commercially available magnetostrictive alloy, Terfenol-D is introduced and its applications are discussed. A novel application of Terfenol-D in controlling the normal load at the friction interface of the bladed disks is proposed in this thesis.

5.1 Historical overview

Magnetostriction can be described as the deformation of a magnetic material caused by a change in its magnetization [66]. The change in magnetization results from magnetic moment rotations, which can be brought about by the application of magnetic fields, heat, or stresses. It is related to various other physical effects [67]. The magnetostriction is a reversible material property and therefore magnetostrictive material returns to its original shape in absence of a magnetic field. Discovery of the magnetostriction goes back to 1842 when Joule observed a slight change in the dimension of an iron rod under an applied magnetic field [68]. He notices a strain ($\Delta L/L$) of 0.7×10^{-6} and assumed the process to be volume conserving. This discovery is known as “Joule magnetostriction” and developed strain is referred to as magnetostrain (λ), see Fig. 2(a) PAPER-D. There are two types of magnetostriction exist in the magnetic materials, called positive and negative. Joule actually observed the negative magnetostriction and with time materials with the positive magnetostriction is discovered. Furthermore, the magnetostriction is in fact not volume conservative as presented in Refs. [69, 70], however the volume change is negligible under normal operation conditions compare to the “Joule magnetostriction”. The inverse of the magnetostriction effect was first discovered in the 1860’s by Villari [71], where applied stress induces a change in magnetization. In other words, the magnetostriction converts magnetic energy to mech-

anical energy and used in actuation application, while Villari effect does the opposite and provides a mechanism for sensing application. Other derived effects of the magnetostriction are “Wiedmann effect” and “Matteucci effect”, see Ref. [72].

All magnetic materials exhibit magnetostriction to some degree; however the giant magnetostriction (magnetostrain $> 1 \times 10^{-3}$) occurs in a small number of materials containing rare earth metals and thus they can be used for practical applications. The most common and commercially available giant magnetostrictive material (GMM) is Terfenol-D, which has a magnetostrain capacity up to 2×10^{-3} . These large strains are a direct consequence of a strong magneto-elastic coupling or magnetoelasticity of GMM. Another manifestation of strong magneto-elastic coupling is a large ΔE effect, a change in elastic modulus accompanying a change in magnetization [73]. The ΔE effect is very small in nickel ($\Delta E = 0.06$), while it is quite large in Terfenol-D ($\Delta E \approx 5$). The ΔE effect of Terfenol-D can be advantageously employed in tunable vibration absorbers and broadband sonar systems [74]. Due to the change of the elastic modulus, there is a change in the velocity of sound inside the magnetostrictive materials and this can be observed. Other details of Terfenol-D are discussed below.

5.2 Giant magnetostrictive material Terfenol-D

Terfenol-D ($\text{Tb}_{0.3}\text{Dy}_{0.7}\text{Fe}_{1.95}$) is an alloy of terbium, iron and dysprosium with high magnetostriction capacity and high Curie temperature (380°C). Terfenol-D has high force capabilities and high strain at off-resonant frequencies and it can operate in the relatively hot environment above room temperature. These properties make it suitable for many commercial applications such as sound and vibration sources, vibration control, sonar systems, underwater information exchange, micromotional control and magnetostrictive motors and many more applications are developing.

As magnetic field passes through Terfenol-D, small magnetic domains rotate and re-orient themselves and that cause the strain in the material, see Fig. 5.1. A stronger magnetic field leads to stronger and more definite re-orientation and finally, leads to the saturation point as seen in Fig. 5.2. The curves in Fig. 5.2 reveal that the negative magnetic field produces the same elongation as the positive magnetic field and the shape of the $\lambda - H$ (magnetostrain vs magnetic field) curve resembles a butterfly and therefore it is referred to as butterfly curve. Note that the $\lambda - H$ curve is highly nonlinear in nature, however a linear relationship exists between the strain and the magnetic field before the saturation region and devices are often designed to operate in this region, see Section 3 PAPER-D for the linear modelling used in this thesis. Actuators using Terfenol-D rod is often designed such that the initial point lies at the beginning of the linear region of the butterfly curve. This requires a magnetic bias (H_b) and prestress in

5.2. GIANT MAGNETOSTRICTIVE MATERIAL TERFENOL-D

the system. The magnetic bias is obtained using the permanent magnets or using a DC current in the solenoid, see Fig. 2 PAPER-D. The prestress is employed to enhance the performance of the actuator since a higher magnetostrain can be obtained with the same strength of the magnetic field if Terfenol-D is under prestress, see Fig. 5.2 and often generated using a spring. Moreover, Terfenol-D element has a very high yield strength in compression compare to the tension, see Table 5.1 and as a consequence, Terfenol-D actuators are operated almost exclusively under a compressive load. Furthermore, the relative permeability of Terfenol-D is higher than of free space and quite low compared to a ferromagnetic material such as soft iron ($\mu_r = 60,000$) and therefore a small hysteresis exist in the $\lambda - H$ curve, see Fig. 5.1, however hysteresis effect is neglected in this study.

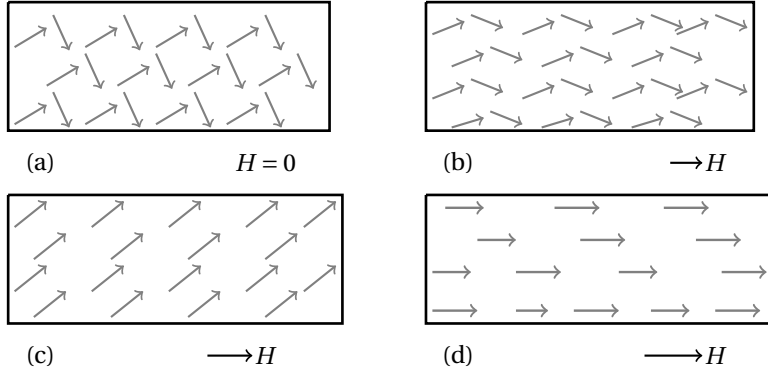


Figure 5.1: Schematic of rotation of magnetic domain with application of magnetic field.

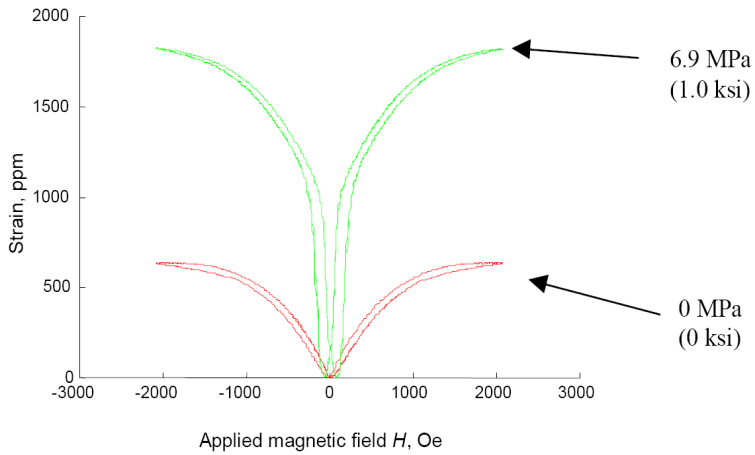


Figure 5.2: Variation in the butterfly curve with preload conditions (6.9 MPa and 0 MPa) [75].

Nominal material properties of Terfenol-D are summarized in Table 5.1. These values can only be used for rough comparisons since the properties are variable in each application. Furthermore, the manufacturing process also has a great influence on the exact value of these properties [76]. Also level of the prestress and the magnetic bias can have a substantial influence on these properties. Therefore, average values of these quantities are used in PAPER-D.

Table 5.1: Material properties of Terfenol-D [76]

Terfenol-D property	Value range	Comments
Nominal composition	$\text{Tb}_x\text{Dy}_{1-x}\text{Fe}_y$	$0.27 < x < 0.3$ & $1.9 < y < 2$
Density	9250 kg/m ³	Depends on the manufacturing
Compressive strength	305–800 MPa	Preferred in applications
Tensile strength	28–40 MPa	Mostly avoided in applications
Elastic modulus	10–75 GPa	At constant H
Sound speed	1640–1940 m/s	Due to ΔE effect
Curie temperature	380°C	Maximum operating temperature
Relative permeability (μ^σ / μ_0)	9.0–12.0	Permeability at constant stress
Saturation magnetization at	1.0 Tesla	Preferred distance to saturation
Magnetostrain	1000–2000 ppm	Parts per million

5.3 Adaptive control of normal load

A novel application of the magnetostrictive actuator is proposed in PAPER-D, where the Joule magnetostriction [77] is employed to increase the normal contact load between the underplatform damper (UPD) and the blade platform of the bladed disk. This is achieved by constraining the actuator between the walls of UPD, see Fig. 6 PAPER-D. Three mounting designs (*ds*g1 to 3) and two boundary conditions between the UPD walls and the actuator output ends are proposed. In the first boundary condition (BC1), there is a frictional contact and in the second boundary condition (BC2), the UPD walls and the actuator ends are bonded. In other words, in the first case, the relative motion between actuator ends and UPD walls is allowed and therefore the normal contact load between the blade platform and the UPD has a contribution from the centrifugal load; whereas in the second case, the UPD is fixed with actuator and therefore the normal contact load between the blade platform and the UPD is only controlled by the actuator force. As the current flows inside the actuator, it expands in the longitudinal direction. However, due to the presence of UPD wall the end displacement is converted into the normal contact load. A static nonlinear contact analysis is

performed to compute the change in the normal load due to different mounting configurations and boundary conditions.

The output force (F_m) and the normal contact load (N_0) on the blade platform as a function of input current for different mounting designs are depicted in Figs. 5.3a and 5.3b for BC1 and BC2, respectively. A detail computational procedure is presented in PAPER-D. The computed results reveal that a change in normal load as high as 750 N can be obtained by properly designing the actuator mounting. It means that change in the normal load can be from 0 to 750 N by varying the input current from 0 to 3 A in the actuator circuit and thus an optimum damping in the system can be achieved by proper tuning of the normal contact load. Furthermore, interface contact parameters such as contact stiffnesses, friction coefficient and contact conditions vary a lot during vibration and therefore optimization of an UPD in the design stage is a demanding task. Alternatively, an optimum damping in the system can be achieved in many cases by changing the normal load even though the interface parameters vary during vibration and with time.

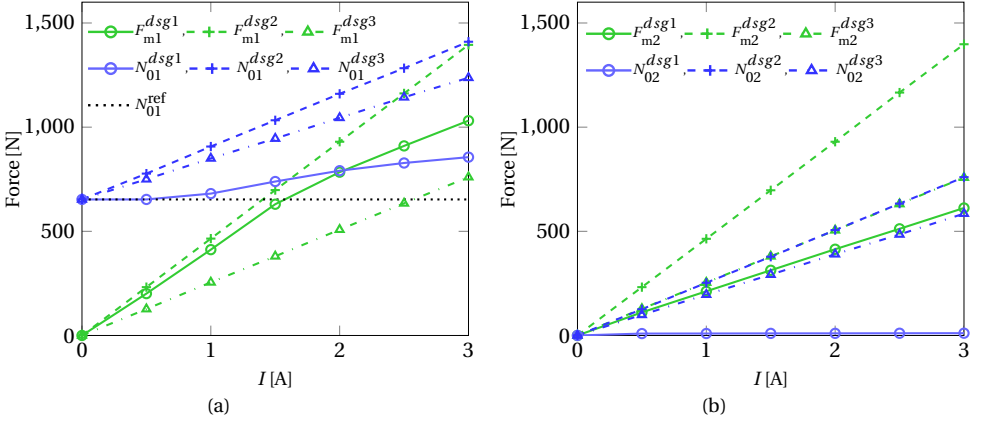


Figure 5.3: Variation in the normal load (N_0) and the output force (F_m) with input current (I) at $\mu = 0.3$: (a) for BC1 and (b) for BC2. N_{01}^{ref} represents the normal load at the blade platform due to the F_c only and N_{01}^{dsg1} represents the normal load due to the F_c and $dsg1$ for BC1. Similarly, N_{02}^{dsg1} represents the normal load due to the $dsg1$ for BC2 and other notations are interpreted in the same way.

5.4 Conclusion

Physics of the magnetostrictive materials is briefly discussed in this chapter. A novel application of the magnetostrictive material Terfenol-D, in controlling the normal contact load at the friction interface of the bladed disks is presented.

CHAPTER 5. MAGNETOSTRICTIVE MATERIALS

6 Results

In this chapter, the time-discrete contact model developed in PAPER-A is applied at the shroud contact, for the nonlinear forced response analysis of a test case bladed disk (Fig. 6.1) and a real bladed disk (Fig. 6.9), by means of the Alternate Frequency Time (AFT) domain method. The contact models selected for these studies have 1D and 2D tangential motion with variable normal load that exhibits turning point bifurcation and induces higher harmonics of the contact forces. The forced response with single harmonic and multiharmonic approximations are presented and compared. Some parametric studies with the variation of normal loads, excitation forces and friction coefficients are also presented in this chapter. The damping potential of strip dampers and multiple friction contacts on a real bladed disk is analyzed and results are presented in PAPER-B and PAPER-C, respectively.

6.1 Test case blade

The test case blade is a simplified bladed disk model consisting of eight sectors, as shown in Fig. 6.1. Blades are coupled by an extended shroud and each sector is discretized into 498 elements with midside nodes using commercial FEM software ANSYS®; the sector comprises 4488 DOFs and 50 mode shapes are kept in the FRF computation, for the receptance based approach in the nonlinear analysis. The nodal diameter map for the bladed disk is shown in Fig. 6.3, in which natural frequencies of most of the mode families (MFs) lie on a horizontal line that indicates blade dominated modes of the bladed disk. A single MF is a group of mode shapes corresponding to the different NDs for the same blade mode since the natural frequencies and mode shapes depend on the ND as explained in chapter 2. The mode shapes of the 1st MF, which corresponds to the first flap (1F) mode of the blade is depicted in Fig. 6.2. The ND = 0 displays inphase motion for all the blades, while ND = 4 exhibits out of phase motion for consecutive blades. For ND = 1 and ND = 2 zero displacement nodal lines are vis-

ible in the figure. Moreover, it should be noted that disk displacement is same for all the NDs, mean disk motion is uncoupled with blade motion and known as blade dominated modes. Furthermore, $ND = 0$ and $ND = 4$ are stationary mode shapes, while $ND = 1, 2$ and 3 are rotating mode shapes.

The coefficient of friction of the contact interface is $\mu = 0.5$, tangential and normal contact stiffnesses are $K_t = 2 \times 10^5 \text{ N/m}$ and $K_n = 10^5 \text{ N/m}$, respectively. The number of discrete points in the FFT computation is 256. In the calculations performed, the steady state amplitude at the response node is computed as $\max(\sqrt{x(t)^2 + y(t)^2 + z(t)^2})$ over one period, where $x(t)$, $y(t)$ and $z(t)$ are the time domain displacements of the response node in the global coordinate system at the sought frequency. The response of the bladed disk is obtained for the 1D and 2D tangential motion with variable normal load in case study-1 and 2, respectively.

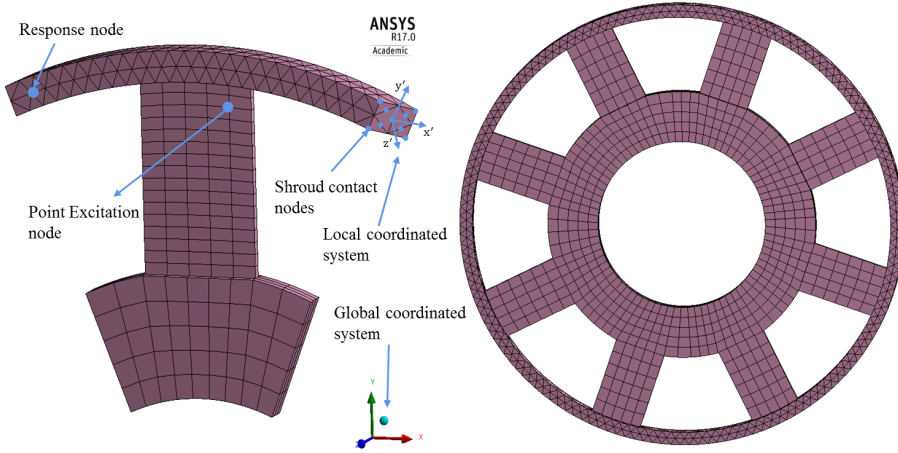


Figure 6.1: Finite element model of the test case blade

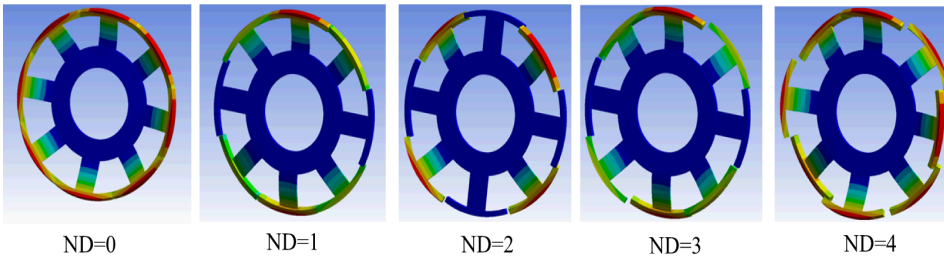


Figure 6.2: Mode shapes of the 1st mode family (1F mode) for different nodal diameters

6.1.1 Case study-1

In this case study, a point excitation $\hat{f}_x = \hat{f}_y = \hat{f}_z = 2\text{N}$ with the spatial periodicity of $m = 3$, which corresponds to engine order (EO)3, is applied at the excitation node of the blade. The static component of the normal load (N_0) is kept constant at 5N and the contact model with the 1D tangential motion and variable normal load is considered in the response computation. The response around the MF1 (1F) mode is analyzed. The excited nodal diameters due to the point excitation and higher harmonics of contact forces are listed in Table. 6.1. Furthermore, excitation temporal harmonics corresponding to the rotational speed of 2800rpm and $m = 3$ is depicted in Fig. 6.3.

Table 6.1: Example for the relation between the number of the temporal harmonics n , spatial harmonics m , the harmonic index h and the nodal diameter ND. $(-)$ and $(+)$ represent the backward and forward travelling wave, respectively.

Engine order = $m = 3$, Number of blades = $n_b = 8$		
Temporal harmonic(n)	Harmonic index = $H = \text{mod}(m * n, n_b)$	Nodal diameter (ND)
1	3	3 ⁽⁻⁾
2	6	2 ⁽⁺⁾
3	1	1 ⁽⁻⁾
4	4	4
5	7	1 ⁽⁺⁾
6	2	2 ⁽⁻⁾
7	5	3 ⁽⁺⁾
8	0	0
9	3	3 ⁽⁻⁾
\vdots	\vdots	\vdots

The response curve obtained with 1,3,5 and 10 harmonics in the EQM are plotted in the Fig. 6.4. A reduction of 1/2.75 times in the peak amplitude is achieved at this load, however this is not the optimum damping in the system, more reduction in the amplitude is obtained at other normal loads. As the number of harmonics in the EQM increases, some additional peaks appear in the low frequency region that corresponds to blade torsion, MF2 (1T) of the bladed disk and it is excited by the second and third harmonics of the contact forces. The higher harmonics of the contact forces are generated due to the stick-slip motion.

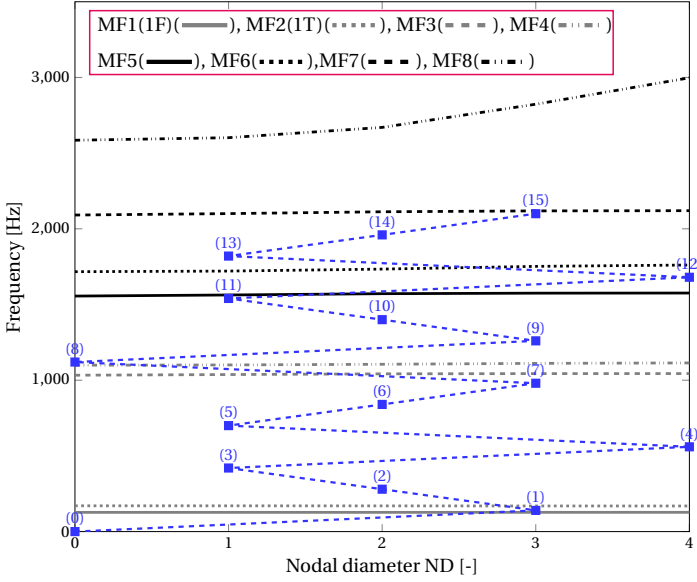


Figure 6.3: Nodal diameter map (ZZENF diagram) of the test case blade with 8 mode families. The blue dashed line with numbers (temporal harmonic (n)) indicates the engine excitation frequencies for the rotation speed of 2800 rpm and $m = 3$.

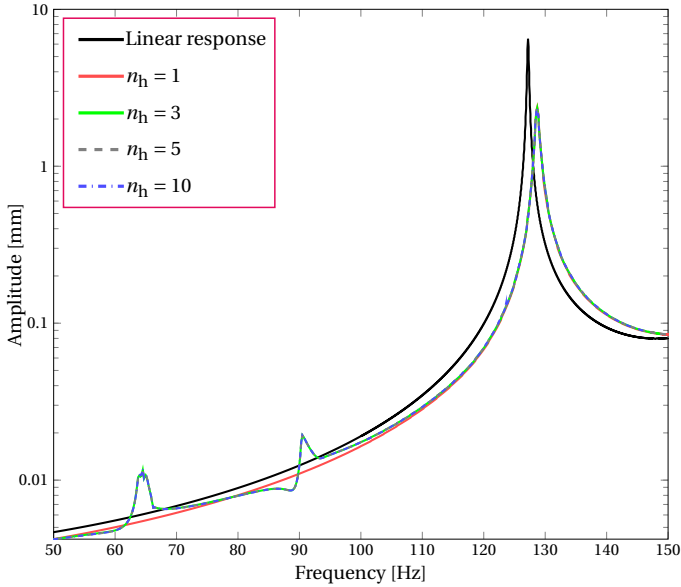


Figure 6.4: Response amplitude of the test case blade at $N_0 = 5$ N and $f = 2$ N with varying n_h .

However, the peak amplitude at the shifted resonance of the 1F mode (128.7Hz) remains unchanged as the number of harmonics increases. This is also observed in the amplitudes of the harmonic component of the displacement in Fig. 6.5, which are dominated by the first harmonic around the 1F mode.

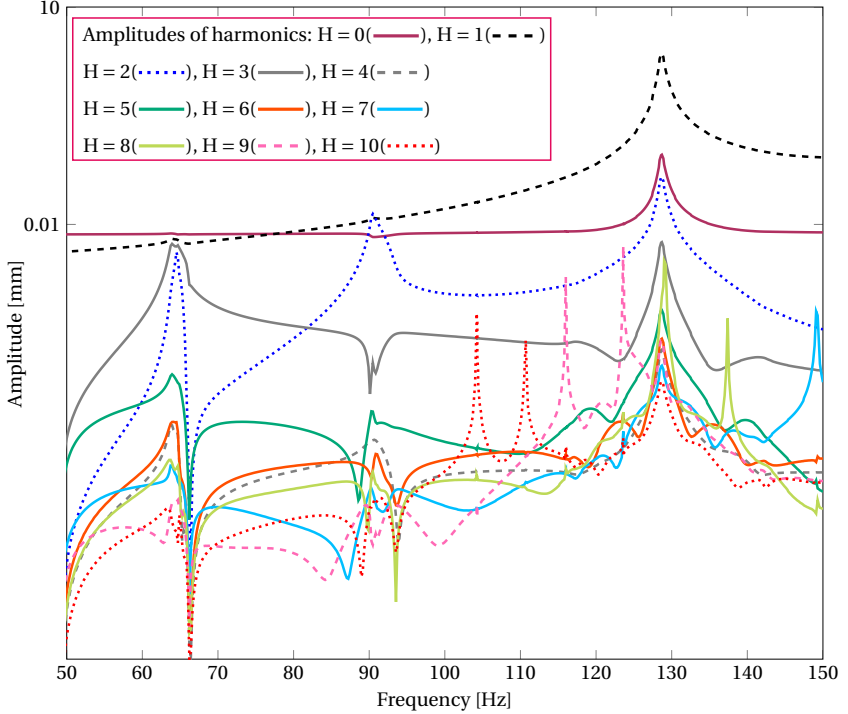


Figure 6.5: Harmonics of the forced response curve of the test case blade at $N_0 = 5$ N and $f = 2$ N.

In Fig. 6.6, the friction force and its harmonic components are plotted for 90.5 Hz and 128.7 Hz. It should be noted that the higher harmonics (2nd and 3rd) of the non-linear tangential force at 128.7 Hz have comparable amplitude to the first harmonic, even though it has no influence on the response amplitude. This is because, there is no resonance frequency close to 2, 3...7th temporal harmonics of the contact forces around 128.7 Hz (2800 rpm, $m = 3$), see nodal diameter map Fig. 6.3. On the other hand, a small magnitude of the second harmonic of the contact force at 90.5 Hz has a significant influence on the vibration amplitude due to the presence of 1T resonance mode at 181 Hz. Furthermore, the peak magnitude of the contact force at 128.7 Hz is 11 N, while the static component of the friction force is 2 N (μN_0) that reveals a huge contribution of the variable component of the normal load. Therefore, in such cases keeping the normal load constant will result in an inaccurate prediction.

CHAPTER 6. RESULTS

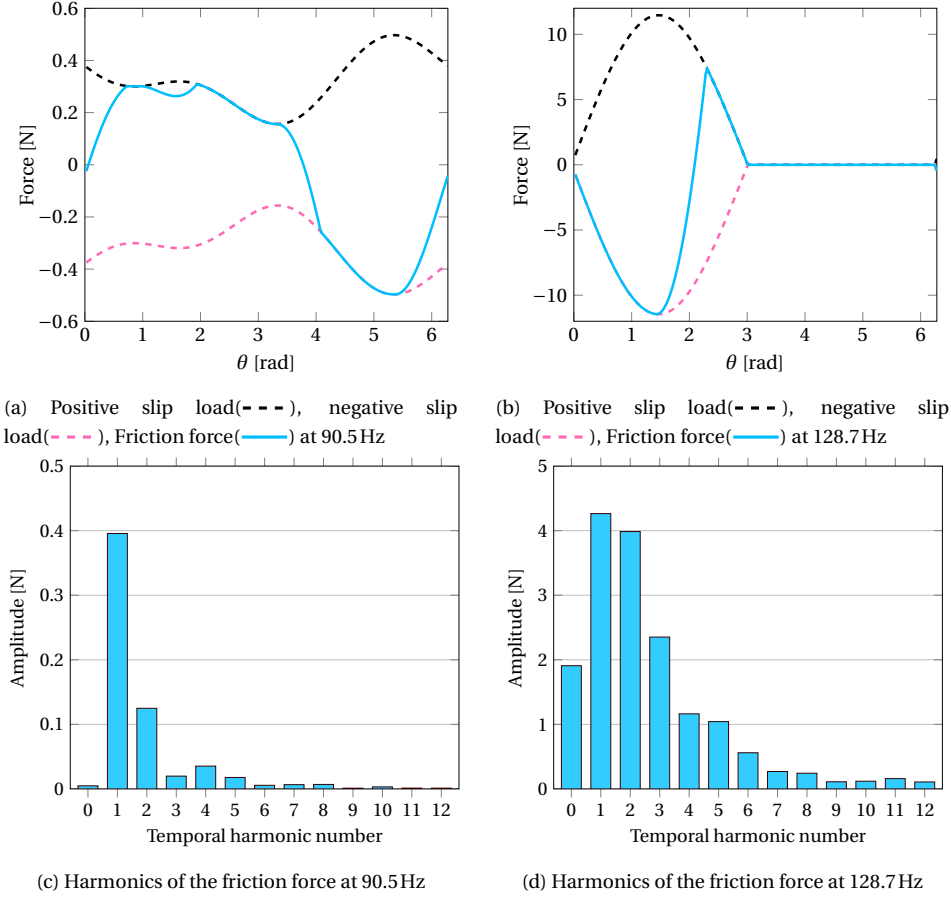


Figure 6.6: Friction forces and their harmonic components.

6.1.2 Case study-2

The excitation force amplitude considered for the second case study is the same as the first, however EO1 is investigated instead of EO3. The full-3D contact model with variable normal load is applied and the response around the first torsion MF2 (1T) is analyzed in this case. The static component of the normal load (N_0) is varied from an initial gap of 1mm to 200N load, to study the behavior of the response curve and to find the optimum normal load for the maximum damping in the system. Five harmonics are retained in the EQM to predict the accurate response of the structure as observed in the previous case. The normal contact stiffness is the same as in the first case and

the tangential contact stiffness reads as,

$$\mathbf{K}_t = \begin{bmatrix} K_t & 0 \\ 0 & K_t \end{bmatrix}. \quad (6.1)$$

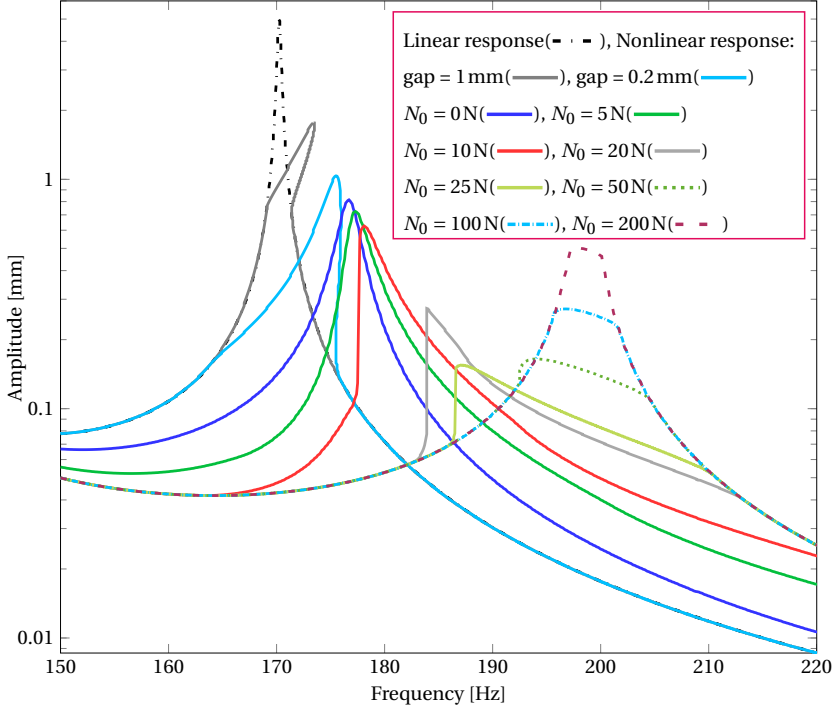
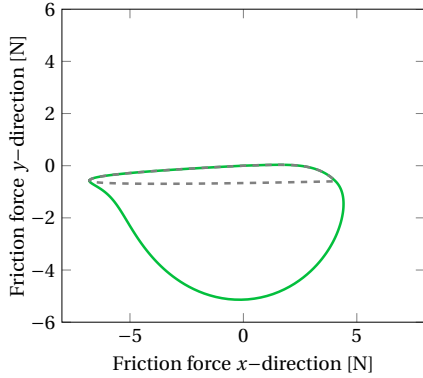


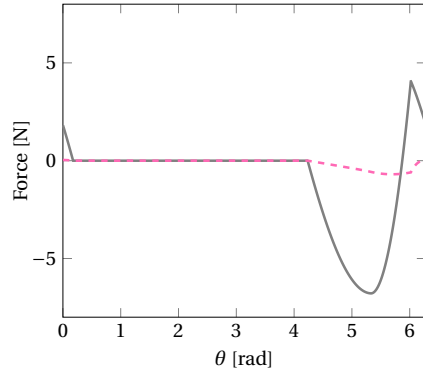
Figure 6.7: The forced response curve obtained around MF2 (1T mode) at $f = 2$ N with varying gap and normal load.

The obtained response curve is depicted in Fig. 6.7. A noticeable variation of the resonance frequency and damping effect is clearly visible. The initial gap in the shroud leads to the turning point bifurcation and it gives a stiffening effect to the structure. The gaps also provide a damping effect to the structure, but it may damage the shroud contact and hence the turbine blade due to impact in each periodic cycle. Furthermore, as the normal load increases peak amplitude drops to a minimum level that is the required value of normal load to achieve the optimum damping in the system, which is around 25 N in this case. At this load, motion of the damper is in the slipping state at most of the time in a periodic cycle. A further increase in the normal load brings the system in stick-slip phase that provides more stiffening effect to the system than damping.

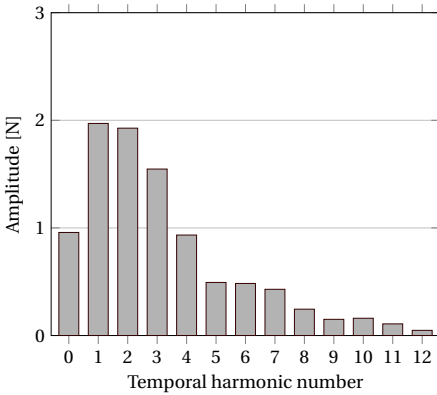
The slip and friction loop at 173.5 Hz for a 0.2 mm gap (turning point) case is presented in Fig. 6.8. It clearly reveals that the predominant direction of motion lies along the x -axis and the amplitude of the tangential force in the y -direction is almost 10 times lower than in the x -direction. Therefore, the motion along the y -axis contributes little to the damping of the system. In these cases, 2D uncoupled friction contact model with variable normal load also lead to an accurate response prediction. A case study with 2D coupled and uncoupled friction contact model is presented in PAPER-A. Furthermore, the tangential force is zero in more than half of the period cycle that is the most likely case around the turning point due to the separation of contact. Therefore, it also generates higher harmonics of the tangential contact forces, as shown in Fig. 6.8. However, these higher harmonics do not effect the nonlinear response curve due to the same as reason explained before.



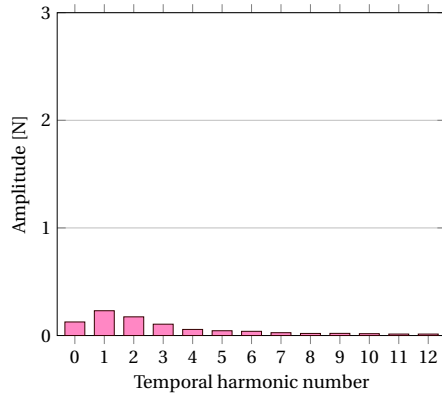
(a) Slip loop(—) and friction loop(---)



(b) Friction force, x -direction(—) and y -direction(---)



(c) Harmonics of friction force in x -direction



(d) Harmonics of friction force in y -direction

Figure 6.8: Friction force and its harmonics at 173.5 Hz and 0.2 mm gap.

6.2 Real bladed disk

One of the low-pressure turbine (LPT) rotor blades that is under investigation inside the COMP project is shown in Fig. 6.9. The rotor blades were designed and manufactured during the FUTURE project (Flutter-free turbomachinery blades, 2009–2012) led by KTH energy technology department and the LPT rotor blade is located at Centro de Tecnologías Aeronáuticas (CTA) facility. Flutter tests and measurements with interlock shroud were performed during the FUTURE project.

One of the aims inside the COMP project is to compare the measurement results with the new developed simulation tool. Therefore, some preliminary simulation results on the CTA rotor blades are presented below.

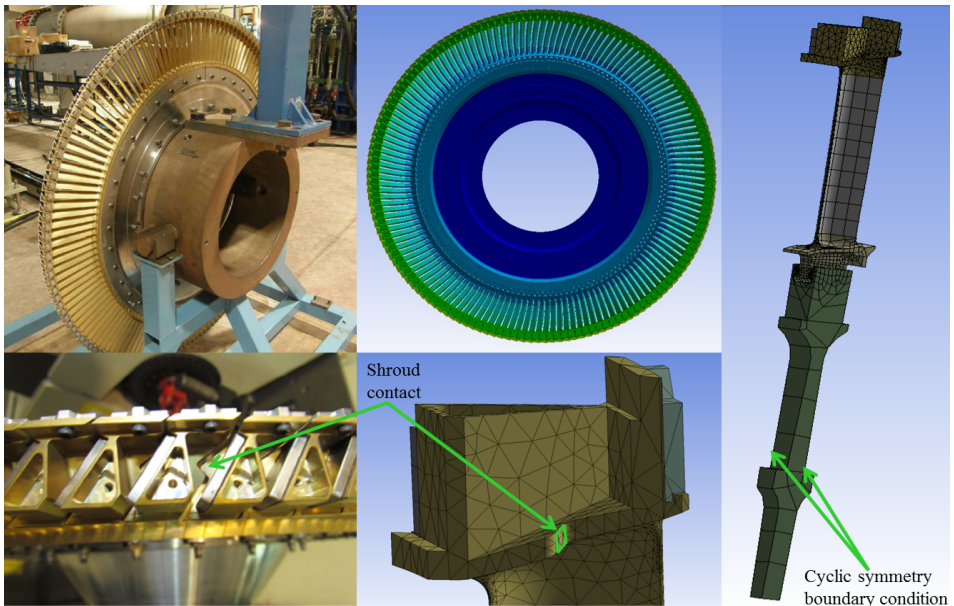


Figure 6.9: Low pressure turbine (LPT) rotor blades at Centro de Tecnologías Aeronáuticas and its FEM model.

The CTA rotor turbine consists of 146 blades and the blades are coupled through an interlock shroud, see Fig. 6.9. Due to the limited capacity of MATLAB®, the blade is coarsely meshed with 32490 DOF. For the generation of the FRF matrix, the first 50 natural frequencies and mass-normalized mode shapes are determined for the required NDs. The nodal diameter map for the first eight mode families of the bladed disk is shown in Fig. 6.10. Unlike the test case blade, natural frequencies of the MFs correspond to the low NDs lie on the curves, that represent the disk dominated modes of

the CTA blades; while natural frequencies correspond to the high NDs are on the horizontal line that indicate the blade dominated mode shapes. In other words, blade/disk motion is coupled for low NDs and uncoupled for the high NDs. Modal damping due to material energy dissipation is assumed to be 0.001. The number of discrete points in the FFT computation is 256.

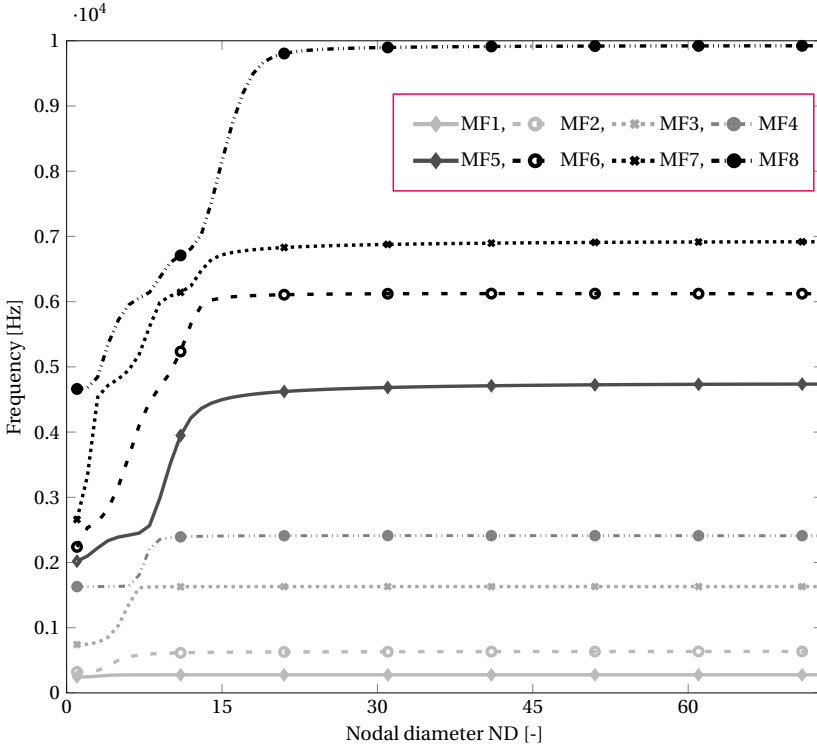


Figure 6.10: Nodal diameter map of the CTA blades.

6.2.1 Case study-3

The CTA blade is excited on the blade tip with a point force ($\hat{f}_x = \hat{f}_y = \hat{f}_z = 1$ N) of EO10 and the response is computed on the shroud tip. The shroud contact interface is shown in Fig. 6.9 and five node-to-node contacts are utilized for the evaluation of the contact forces. The full-3D contact model with variable normal load is applied and the response around the first MF is analyzed here. The aim of the case study is to demonstrate the capability of the developed simulation tool in describing the complex friction contact on a real bladed disk and compute the nonlinear response curve with multiple contact nodes at the friction interface. The normal contact stiffness is $K_n = 1 \times 10^6$ N/m and the

tangential contact stiffness reads as,

$$\mathbf{K}_t = \begin{bmatrix} 2 \times 10^6 & 0 \\ 0 & 2 \times 10^6 \end{bmatrix} \text{ N/m.} \quad (6.2)$$

Results of the forced response calculation, obtained for three load cases (0.05 mm gap, 5 N and 10 N load) with varying number of the temporal harmonics (1, 2, 5 and 10) is presented in Fig. 6.11. A slight change in resonance frequency is observed for all loads and a significant damping effect is found even in the case of a gap. The behavior of the response curve is similar to the test case blade, with a decrease of the response amplitude as the normal load increases. Results for the different number of harmonics in the EQM are shown in the figure. Practically identical response curves are obtained with 5 and 10 harmonics in the EQM. Therefore, we can conclude that the response converges for 5 harmonics in this case. However, single harmonic balance is assumed in the next computations.

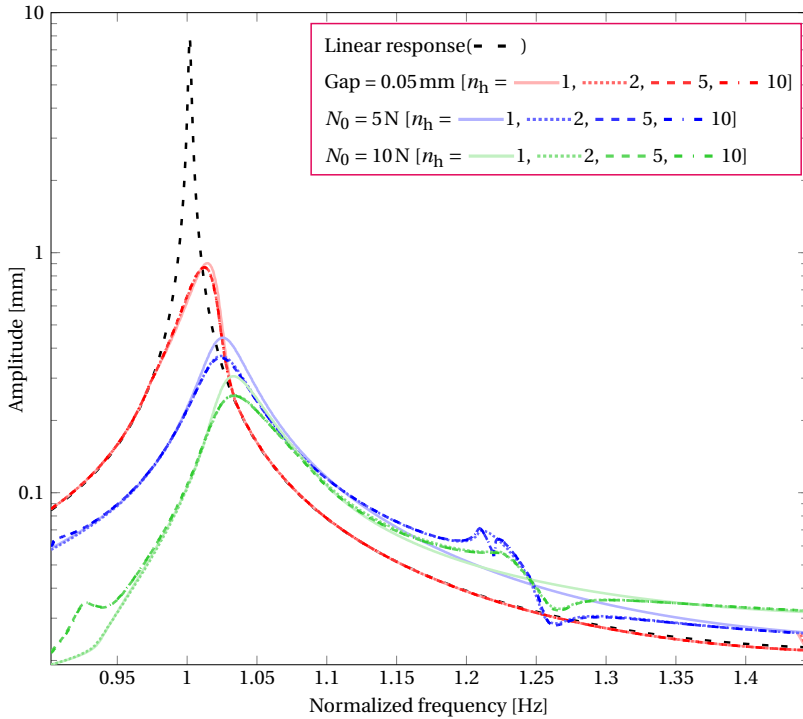


Figure 6.11: The forced response curve for the CTA blade at varying gap, normal load and number of harmonics.

In Fig. 6.12, the frequency response function (FRF) with varying excitation level is plotted. The damping effect for the all the excitation levels is evident from the curve. At

small excitation level, the shroud is in the sticking state and due the high contact stiffness assumed in the simulation, a large shift in the resonance frequency is observed. As the excitation level increases, more slipping takes place in the contact and hence resonance frequency moves close to the free standing natural frequency of the shroud. At $f = 0.3\text{ N}$, maximum damping is achieved in this case, however net damping in the system is a function of the ratio $\mu N_0/f$, while K_n and K_t are kept constant.

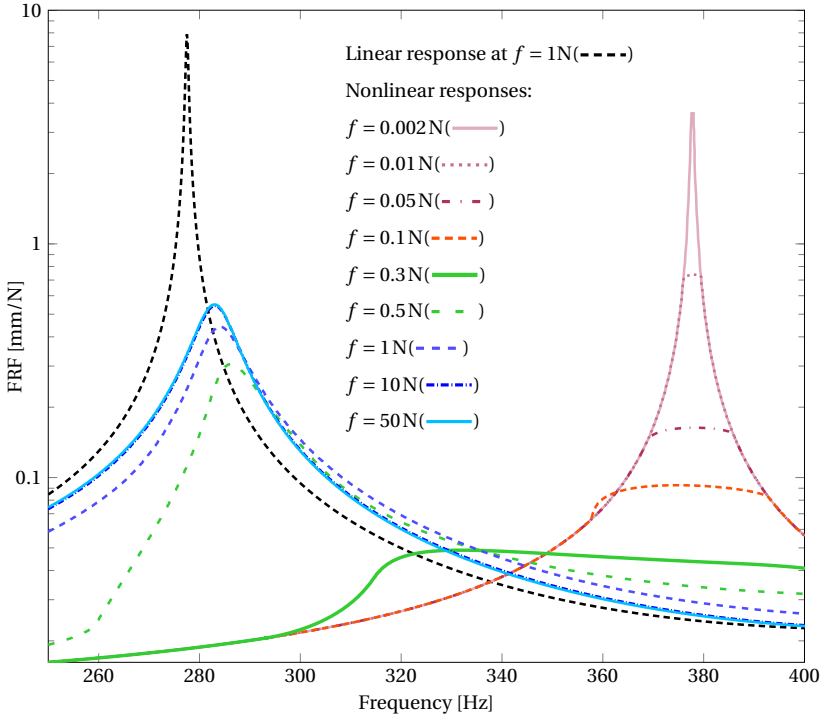


Figure 6.12: The nonlinear frequency response function of the CTA blade obtained at varying excitation amplitude ($\mu = 0.4$ and $N_0 = 5\text{ N}$).

Forced response level calculated for the nominal excitation level ($f = 1\text{ N}$), but with different values of friction coefficient are shown in Fig. 6.13. The response curve behavior resembles a single degree of freedom system with varying viscous damping level. A little change in the resonance frequency is observed at this normal load and excitation level. However, the effect on the amplitude is significant.

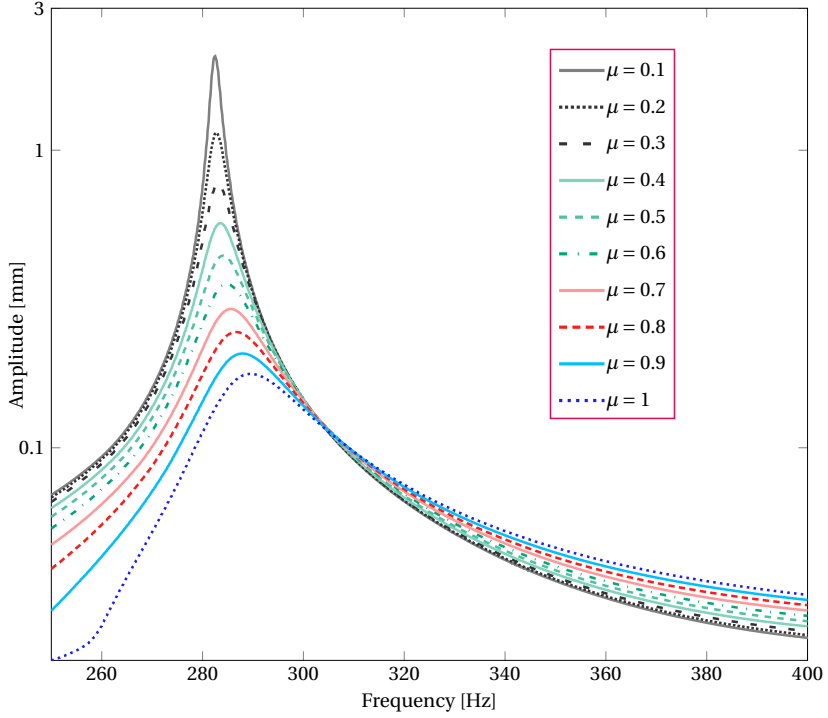


Figure 6.13: Influence of friction coefficient variations on the nonlinear forced response of the CTA blade computed at $f = 1$ N and $N_0 = 5$ N.

6.3 Conclusion

The dependency of the resonance frequencies and resonance amplitudes on the normal loads, excitation forces and the contact interface parameters (K_n , K_t and μ) are presented in this chapter. The results obtained illustrate the complicated features exhibited by the friction contact on the forced response of the bladed disk. The nonlinear nature of the friction contact generates higher harmonics of the friction force that requires multiharmonic formulation of the EQM. An increase in the number of harmonics also increases the size of the EQM and therefore increase the computation time. A comparative study reveals that 5 harmonics are enough in the above examples to capture the response accurately with negligible error. However, the number of harmonics required depends on the dynamics of structure, excitation forces and on the contact model. First few simulations can be used to decide upon the number of harmonics required for the accurate prediction, before running the parametric studies.

The obtained results reveal that despite the strong nonlinearities exhibited by the

CHAPTER 6. RESULTS

friction contact, see Fig. 6.6 and 6.8, the developed numerical simulation tool (WP3) is capable of solving the nonlinear system of equations over a wide frequency range without being hindered by convergence problems. Therefore the developed tool seems to be effective for the study of dynamic systems featuring complex nonlinear contact forces. Furthermore, comparative analysis of the test case and the real bladed disks also reveals that as the number of DOFs increases in the analysis, computation time becomes larger, therefore reduce order modelling (WP1) must be integrated with WP3 to perform the parametric studies on industrial bladed disks. Finally, for a given structure, the net damping in the system is a function of $\mu N_0 / f$, therefore in order to obtain the maximum damping response curve should be minimized with respect to $\mu N_0 / f$.

7 Conclusions and Recommendations for Future Work

7.1 Concluding remarks

Accurate modelling of friction contact and solution of the resulting nonlinear algebraic equations in a reasonable time are of vital importance for the industrial application of the numerical simulation tool developed to study friction damping of bladed disks. A simple 1D contact model yields fast results, but it is not accurate enough to capture the full-3D motion of the contact interface and hence it underestimates or overestimates the amount of friction damping. Furthermore, friction damping depends on many parameters such as rotational speed, engine excitation order, normal contact load, contact stiffness and friction coefficient values etc. Moreover, contact stiffness values are the function of the normal contact load, contact area, contact geometry, etc. and varies significantly during operation. In conclusion, it is very hard to estimate and control the contact interface parameters and therefore accurate prediction of the nonlinear forced response curve is not an easy task. This thesis attempts to answer few of these challenges and the main output and conclusions of this thesis work are:

⇒ A 3D time-discrete contact model is reformulated and an analytical expression to compute its Jacobian matrix is derived in this work. The Jacobian matrix is calculated in parallel with the computation of the nonlinear contact force in the AFT framework leading to a more efficient approach than to the classical finite difference approach. The contact model and the dynamics of bladed disks are encrypted in MATLAB[®] and a simulation tool to study the friction damping on bladed disks is developed during the project. The tool has a capability to simulate shroud contact, underplatform damper and multiple friction contacts as well.

CHAPTER 7. CONCLUSIONS AND RECOMMENDATIONS FOR FUTURE WORK

⇒ The numerical studies performed using the developed tool reveal that despite the strong nonlinearities exhibited by the friction contact, the tool is capable of solving the nonlinear system of equations over a wide frequency range without being hindered by convergence problems. Therefore the developed tool seems to be effective for the study of dynamic systems featuring complex nonlinear contact forces.

⇒ A comparison between quasi-3D and full-3D contact model reveals that the quasi-3D contact model leads to an over and underestimation of friction damping in the general case and a full-3D friction contact model is essential to accurately predict the nonlinear forced response of a bladed disk.

⇒ A numerical investigation of the strip dampers indicates that a significant amount of damping in the system can be achieved with a very thin strip (Thickness = 0.5 mm and mass = 2 gram) due to the high normal load induced by the centrifugal forces. Furthermore, the strip damper is more efficient for low nodal diameters, where blade-disk motion is strongly coupled.

⇒ Numerical investigation of multiple friction contacts reveals that friction damping obtained using multiple contact interfaces is additive in nature and harvest the benefit of all the contact interfaces. By using multiple friction contact interfaces several nodal diameters and modal families can be damped simultaneously in a wider range of engine excitation amplitude, this is in contrast to the case with a single friction interface.

⇒ The nonlinear nature of the friction force leads to higher harmonics of the contact force, that require a multiharmonic formulation of the EQM. However, an increase in the number of harmonics also increases the size of the EQM and therefore the computation time. A comparative study in chapter 6 and PAPER-A, reveals that 5 harmonics are enough to capture the response accurately with negligible error. However, the number of harmonics required depends on the dynamics of structure, excitation and on the contact model. First few simulations can be used to decide upon the number of harmonics required for an acceptable accurate solution, before running the parametric studies.

⇒ Finally, a novel application of the giant magnetostrictive material in adaptive control of the normal contact load at the friction interface of a bladed disk is proposed. The numerical investigation reveals that the change in the normal load as high as 750 N can be obtained by properly designing the actuator mounting. It means that change in the

normal load can be from 0 to 750 N by varying the input current from 0 to 3 A in the actuator circuit and thus an optimum damping in the system can be achieved by proper tuning of the normal contact load.

7.2 Recommendations for future work

The computation of FRF matrix at each iteration step also consumes a substantial amount of time with many contact nodes. A reduction method with high-accuracy FRF developed in Ref. [38] is integrated with the developed simulation tool to reduce this time. However, a further decrease in the computation time can be achieved by employing the component mode synthesis techniques (WP1) in the formulation of the EQM, especially for the nonlinear analysis of a mistuned system. Therefore, it is highly recommended to integrate WP1 with WP3 to enhance the computational potential of the developed tool.

The simulated nonlinear forced response curve are the function of contact interface parameters, mainly the contact stiffness and the friction coefficient (K_n , K_t and μ). These parameters are material dependent and vary substantially with the variation of normal contact load, contact geometry, contact area, temperature, etc. Furthermore, the contact area can significantly change due to vibrations of the blades. Therefore, these parameters are required to be understood in the better way particularly for a flat-on-flat contact in order to use the developed tool with confidence. Furthermore, the validation of the developed simulation tool is also required. For example, two blades model with strip damper can be considered to validate the result of PAPER-B and in parallel, the influence of the strip thickness and the contact area on the interface parameters can be investigated. A comparative study of the wedge dampers and the strip dampers can also be performed on the same test bench. The centrifugal load is often higher than the required value due to the high rotational speed of the bladed disk and it can be reduced by some factors if strip damper can be used instead of the widely used rigid wedge dampers.

Finally, the innovative solution proposed in PAPER-D should be validated experimentally and its practical application possibilities should be explored.

CHAPTER 7. CONCLUSIONS AND RECOMMENDATIONS FOR FUTURE WORK

8 Summary of Appended Papers

PAPER-A: An analytical calculation of the Jacobian matrix for 3D friction contact model applied to turbine blade shroud contact

In PAPER-A, an analytical expression is formulated to compute the Jacobian matrix for 3D friction contact modelling that efficiently evaluates the matrix while computing the friction contact forces in the time domain. The analytical expression drastically reduces the computation time of the Jacobian matrix with respect to the classical finite difference method. Alternate frequency time domain method is used to switch between the frequency domain equations of motion and the computation of the nonlinear force in the time domain at discrete time steps. The method allows capturing complex nonlinearities exhibited by the friction forces and the normal forces while keeping the computational advantage of frequency domain modelling.

The developed expression is successfully used for the calculation of the friction damping on a bladed disk with shroud contact and a comparison between quasi-3D and full-3D contact model is presented. The numerical investigations show that the quasi-3D and full-3D friction contact models result in similar results if tangential motion in the shroud contact plane occurs mainly along one axis, whereas if the tangential motion is either 2D or 1D but not dominated along one axis in the chosen shroud local coordinate system, then the quasi-3D formulation leads to an over and underestimation of friction damping. Since the motion kinematics in the shroud contact plane is seldom known in advance, therefore the full-3D friction contact model is essential to accurately predict the nonlinear forced response of a real bladed disk.

Furthermore, the computation time of the analytical Jacobian is compared with the finite difference method. The comparison shows that the computational time with a single contact node is equal for both methods; however, as the number of contact nodes increases a substantial amount of time saving (70% with 5 contact nodes) is

achieved by using the analytical method. Therefore, it can be argued that the proposed method is more beneficial for the case of mistuned assemblies and for the simulation of microslip behavior using multiple contact nodes at the interface. In addition, it is also noticed that the quasi-3D formulation requires 40% less time compared to the full-3D formulation, therefore the quasi-3D formulation should be used where applicable.

PAPER-B: Investigation of damping potential of strip damper on a real turbine blade

PAPER-B investigates the damping potential of a strip damper on a real bladed disk. A finite element model of the strip dampers that allows for an accurate description of their dynamic properties is included in the steady-state forced response analysis of the bladed disk. The strip damper is modelled with (a) free-free and (b) elastic boundary conditions and their influences on the nonlinear forced response curve are analyzed.

Practically no difference due to a change in the boundary condition of the strip is observed on the blade response curves, and therefore it is suggested that both boundary conditions can be employed in the nonlinear analysis of bladed disks with strip dampers. Furthermore, the effect of the strip thickness and the mass are also investigated. The computed results reveal that a significant amount of damping in the system can be achieved with a very thin strip (Thickness = 0.5 mm and mass = 2 gram) due to the high normal load induced by the centrifugal forces. Furthermore, the effect of the strip damper on different nodal diameters of modal family 2 is analyzed. The obtained results reveal that the strip is more efficient for low nodal diameters, where blade-disk motion is strongly coupled, however a moderated amplitude reduction (50%) is observed for high nodal diameters as well.

PAPER-C: Numerical analysis of multiple friction contacts in bladed disks

In PAPER-C, the effect of multiple friction contact interfaces (shroud contact + strip damper) on the nonlinear forced response of a realistic bladed disk is investigated and results are compared with the single friction contact interface (shroud contact or strip damper). The obtained results reveal that friction damping obtained using multiple contact interfaces is additive in nature and harvest the benefit of all the contact interfaces. By using multiple friction contact interfaces several nodal diameters and modal families can be damped simultaneously in a wider range of engine excitation amplitude, this is in contrast to the case with a single friction interface. Therefore, multiple friction contact interfaces are a potentially effective solution if several critical resonances are present in the operating frequency range, which is often the case for a real

bladed disk. Furthermore, a highly accurate definition of the FRF matrix is employed in the analysis that is capable of representing the accurate dynamics of the structure with few dynamic modes by capturing the static residual stiffness separately. This reduces the computation time substantially while the dynamics of the structure are represented accurately especially the local elasticity of the friction interface that is essential to compute the nonlinear contact forces. Furthermore, a combination of highly accurate-FRF matrix and an analytical calculation of the Jacobian matrix (PAPER-A) simulate the multiple friction contacts of a complex bladed disk in a reasonable time and therefore the method is potentially applicable in the design phase at the industrial level as well.

PAPER-D: Adaptive control of normal load at the friction interface of bladed disks using giant magnetostrictive material

In PAPER-D, a novel application of magnetostrictive actuators in underplatform dampers of bladed disks is proposed for adaptive control of the normal load at the friction interface in order to achieve the desired friction damping in the structure. Friction damping in a bladed disk depends on many parameters such as rotational speed, engine excitation order, nodal diameter, contact stiffness, friction coefficient and normal contact load. However, all these parameters have a fixed value at an operating point. On the other hand, the ability to vary some of these parameters such as the normal contact load is desirable in order to obtain an optimum damping in the bladed disk at different operating conditions. This is achieved by constraining the output rod of the actuator between the walls of the underplatform damper.

The computed results reveal that a change in normal load as high as 750N can be obtained by properly designing the actuator mounting. It means that change in the normal load can be from 0 to 750N by varying the input current from 0 to 3A in the actuator circuit and thus an optimum damping in the system can be achieved despite a variation in the contact interface parameters during vibration. Moreover, two boundary conditions (BC1 and BC2) between the actuator ends and the UPD walls are proposed, where the BC1 is potentially applicable where a high normal load is required to achieve the optimum damping in the system and the BC2 is recommended for a low normal load case. Furthermore, it is demonstrated that the friction coefficient has a significant influence on the normal contact load and thus on the nonlinear vibration prediction of the bladed disk with friction contact. Finally, it is possible to damp several resonances at different operating conditions by altering the normal load at the friction interface.

CHAPTER 8. SUMMARY OF APPENDED PAPERS

Bibliography

- [1] J. H. Griffin, A review of friction damping of turbine blade vibration, *International Journal of Turbo and Jet Engines* 7 (1990) 297–307.
- [2] T. M. Cameron, J. H. Griffin, R. E. Kielb, T. M. Hoosac, An integrated approach for friction damper design, *ASME Journal of Vibration and Acoustic* 112 (1990) 175–182.
- [3] A. V. Srinivasan, D. G. Cutts, Dry friction damping mechanisms in engine blades, *ASME Journal of Engineering for Power* 105 (1983) 332–341.
- [4] G. Csaba, Forced response analysis in time and frequency domains of a tuned bladed disk with friction dampers, *Journal of Sound and Vibration* 214(3) (1998) 395–412.
- [5] A. A. Ferri, E. H. Dowell, Frequency domain solution to multi-degree-of-freedom, dry friction damp systems, *Journal of sound and vibration* 124(2) (1988) 207–224.
- [6] E. Cigeroglu, N. An, C. H. Menq, A microslip friction model with normal load variation induced by normal motion, *Nonlinear dynamics* 50 (2007) 609–626.
- [7] E. P. Petrov, D. J. Ewins, Analytical formulation of friction interface elements for analysis of nonlinear multiharmonic vibrations of bladed disks, *ASME Journal of Turbomachinery* 125 (2003) 364–371.
- [8] O. Poudou, C. Pierre, Hybrid frequency-time domain methods for the analysis of complex structural systems with dry friction damping, in: 44th AIAA/ASME/ASCE/AHS Structural Dynamics and Materials Conference, 7-10 April 2003, Norfolk, Virginia, 2003.
- [9] E. P. Petrov, A method for use of cyclic symmetry properties in analysis of non-linear multiharmonic vibrations of bladed disks, *ASME Journal of Engineering for Gas Turbine and Power* 126 (2004) 175–183.

BIBLIOGRAPHY

- [10] C. Siewert, L. Panning, J. Wallaschek, C. Richter, Multiharmonic forced response analysis of a turbine blading coupled by nonlinear contact forces, *ASME Journal of Engineering for Gas Turbines and Power* 132 (2010) 082501 (9 pages).
- [11] C. H. Menq, J. H. Griffin, A comparison of transient and steady state finite element analyses of the forced response of a frictionally damped beam, *ASME Journal of Vibration, Acoustics, Stress, and Reliability in Design* 107 (1985) 19–25.
- [12] K. Y. Sanliturk, M. Imregun, D. J. Ewins, Harmonic balance vibration analysis of turbine blades with friction dampers, *ASME Journal of Vibration and Acoustic* 119 (1997) 96–103.
- [13] B. D. Yang, J. J. Chen, C. H. Menq, Prediction of resonant response of shrouded blades with three-dimensional shroud constraint, *ASME Journal of Engineering for Gas Turbines and Power* 121 (1999) 523–529.
- [14] K. Y. Sanliturk, D. J. Ewins, A. B. Stanbridge, Underplatform dampers for turbine blades: Theoretical modeling, analysis and comparison with experimental data, *ASME Journal of Engineering for Gas Turbines and Power* 123 (2001) 919–929.
- [15] E. Cigeroglu, H. N. Ozguven, Nonlinear vibration analysis of bladed disks with dry friction dampers, *Journal of Sound and Vibration* 295 (2006) 1028–1043.
- [16] E. P. Petrov, D. J. Ewins, Effects of damping and varying contact area at blade-disk joints in forced response analysis of bladed disk assemblies, *ASME Journal of Turbomachinery* 128 (2006) 403–410.
- [17] S. Zucca, J. Borrajo, M. M. Gola, Forced response of bladed disks in cyclic symmetry with underplatform dampers, in: Paper GT2006-90785, Proceedings of ASME Turbo Expo 2006, May 8–11, Barcelona, Spain, 2006.
- [18] M. Krack, L. Panning, C. Siewert, Multiharmonic analysis and design of shroud friction joints of bladed disks subject to microslip, in: Proceedings of ASME IDETC/CIE, August 12–15, 2012, Chicago, IL, USA, 2012.
- [19] M. Krack, L. Salles, F. Thouverez, Vibration prediction of bladed disks coupled by friction joints, *Archives of Computational Methods in Engineering* (2016) 1–48.
- [20] J. H. Griffin, Friction damping of resonant stresses in gas turbine engine airfoils, *Journal of Engineering for Power* 102 (1980) 329–333.
- [21] C. H. Menq, J. H. Griffin, J. Bielak, The influence of a variable normal load on the forced vibration of a frictionally damped structure, *ASME Journal of Engineering for Gas Turbines and Power* 108 (1986) 300–305.

- [22] B. D. Yang, C. H. Menq, Modelling of friction contact and its application to the design of shroud contact, *ASME Journal of Engineering for Gas Turbines and Power* 119 (1997) 958–963.
- [23] S. Nacivet, C. Pierre, F. Thouverez, L. Jezequel, A dynamic lagrangian frequency-time method for the vibration of dry-friction-damped systems, *Journal of Sound and Vibration* 265 (2003) 201–219.
- [24] D. Charleux, C. Gibert, F. Thouverez, J. Dupeux, Numerical and experimental study of friction damping in blade attachments of rotating bladed disks, *International Journal of Rotating Machinery* 2006 (71302) (2006) 1–13.
- [25] A. Herzog, M. Krack, L. P. Scheidt, J. Wallaschek, Comparison of two widely used frequency-time domain contact models for the vibration simulation of shrouded turbine blades, in: *Paper GT2014-26226, Proceedings of ASME Turbo Expo 2014*, June 16–20, Dusseldorf, Germany, 2014.
- [26] D. Laxalde, F. Thouverez, J. P. Lombard, Forced response analysis of integrally bladed disks with friction ring dampers, *ASME Journal of Vibration and Acoustic* 132(1) (2010) 011013 (9 pages).
- [27] P. R. Dahl, Solid friction damping of mechanical vibrations, *AIAA Journal* 14 (1976) 1675–1682.
- [28] D. J. Segalman, A four-parameter Iwan model for lap-type joints, *Journal of Applied Mechanics* 72(5) (2005) 752–760.
- [29] L. L. Gaul, R. R. Nitsche, The role of friction in mechanical joints, *ASME. Appl. Mech. Rev.* 54(2) (2001) 93–106.
- [30] C. H. Menq, J. H. Griffin, J. Bielak, The influence of microslip on vibratory response, Part2—Comparison with experimental result, *Journal of Sound and Vibration* 107 (1986) 295–307.
- [31] C. H. Menq, J. H. Griffin, J. Bielak, The influence of microslip on vibratory response, Part1—A new microslip model, *Journal of Sound and Vibration* 107(2) (1986) 279–293.
- [32] E. Cigeroglu, W. Lu, C. Menq, One-dimensional dynamic microslip friction model, *Journal of Sound and Vibration* 292 (2006) 881–898.
- [33] I. L. Arteaga, , J. M. Busturia, H. Nijmeijer, Energy dissipation of a friction damper, *Journal of Sound and Vibration* 278 (2004) 539–561.

BIBLIOGRAPHY

- [34] I. L. Arteaga, H. Nijmeijer, Prediction and validation of the energy dissipation of a friction damper, *Journal of Sound and Vibration* 328 (2009) 396–410.
- [35] W. Sextro, *Dynamical contact problems with friction—models, methods, experiments and applications*, Springer, 2007.
- [36] K. Y. Sanliturk, D. J. Ewins, Modelling two-dimensional friction contact and its application using harmonic balance method, *Journal of Sound and Vibration* 193(2) (1996) 511–523.
- [37] S. Yajie, H. Jie, Z. Zigen, Forced response analysis of shrouded blades by an alternating frequency/time domain method, in: Paper GT2006-90595, *Proceedings of ASME Turbo Expo 2006*, May 8-11, Barcelona, Spain, 2006.
- [38] E. P. Petrov, A high-accuracy model reduction for analysis of nonlinear vibrations in structures with contact interfaces, *ASME Journal of Engineering for Gas Turbine and Power* 133 (2011) 102503 (10 pages).
- [39] C. Siewert, M. Krack, L. Panning, J. Wallaschek, The nonlinear analysis of the multiharmonic forced response of coupled turbine blading, in: *IS-ROMAC12-2008-20219*, 2008.
- [40] W. Gu, Z. Xu, Y. Liu, A method to predict the nonlinear vibratory response of bladed disc system with shrouded dampers, in: *Proceeding of the IMechE Vol. 226 Part C: Journal of Mechanical Engineering Science*, 2011.
- [41] J. M. Borrajo, S. Zucca, M. M. Gola, Analytical formulation of the Jacobian matrix for nonlinear calculation of the forced response of turbine blade assemblies with wedge friction dampers, *International Journal of Non-Linear Mechanics* 41 (2006) 1118–1127.
- [42] [link].
URL <http://www.turbokraft.se/>
- [43] S. J. Wildheim, Excitation of rotationally periodic structures, *Journal of Applied Mechanics* 46 (1979) 878–882.
- [44] D. L. Thomas, Dynamics of rotationally periodic structures, *International Journal for Numerical Methods in Engineering* 14 (1979) 81–102.
- [45] B. D. Yang, C. H. Menq, Characterization of 3D contact kinematics and prediction of resonant response of structures having 3D frictional constraint, *Journal of Sound and Vibration* 217(5) (1998) 909–925.

- [46] O. Tanrikulu, H. N. Ozguven, Forced harmonic response analysis of nonlinear structures using describing functions, *American Institute of Aeronautics and Astronautics* 31-(7) (1993) 1313–1320.
- [47] A. Cardona, A. Lerusse, M. Geradin, Fast Fourier nonlinear vibration analysis, *Computational Mechanics* 22 (1998) 128–142.
- [48] M. Urabe, Galerkin's procedure for nonlinear periodic systems, *Archive for Rational Mechanics and Analysis* 20 (2) (1965) 120–152.
- [49] B. D. Yang, C. H. Menq, Nonlinear spring resistance and friction damping of frictional constraints having two-dimensional motion, *Journal of Sound and Vibration* 217 (1998) 127–143.
- [50] W. Gu, Z. Xu, 3D numerical friction contact model and its application to nonlinear blade damping, in: Paper GT2010-22292, *Proceedings of ASME Turbo Expo 2010*, June 14-18, Glasgow, UK, 2010.
- [51] A. Sinha, J. H. Griffin, Effects of static friction on the forced response of frictionally damped turbine blades, *ASME Journal of Engineering for Gas Turbine and Power* 106 (1984) 65–69.
- [52] J. H. Wang, W. K. Chen, Investigation of the vibration of a blade with friction damper by HBM, *Journal of Engineering for Gas Turbines and Power* 115 (1993) 294–299.
- [53] C. H. Menq, P. Chidamparam, J. H. Griffin, Friction damping of two-dimensional motion and its application in vibrational control, *Journal of Sound and Vibration* 144(3) (1991) 427–447.
- [54] E. Cigeroglu, N. An, C. H. Menq, Forced response prediction of constrained and unconstrained structures coupled through friction contacts, *ASME Journal of Engineering for Gas Turbine and Power* 131 (2009) 022505 (11 pages).
- [55] T. M. Cameron, J. H. Griffin, An alternating frequency/time domain method for calculating the steady state response of nonlinear dynamics systems, *Journal of Applied Mechanics* 56 (1989) 149–154.
- [56] K. L. Johnson, *Contact Mechanics*, Cambridge University Press, Cambridge, 1989.
- [57] R. D. Mindlin, M. P. Mason, T. F. Osmer, H. Deresiewicz, Effects of an oscillating tangential force on the contact surfaces of elastic spheres, in: *Proceedings of the First U. S. National Congress of Applied Mechanics*, 1952, pp. 203–208.

BIBLIOGRAPHY

- [58] J. Szwedowicz, B. Ravindra, M. Kissel, R. Kellerer, Estimation of contact stiffness and its role in the design of a friction damper, in: Paper 2001-GT-0290, Proceedings of ASME Turbo Expo 2001, June 4-7, New Orleans, 2001.
- [59] C. Siewert, L. Panning, A. Schmidt-Fellner, A. Kayser, The estimation of the contact stiffness for directly and indirectly coupled turbine blading, in: Paper GT2006-90473, Proceedings of ASME Turbo Expo 2006, May 8-11, Barcelona, Spain, 2006.
- [60] K. H. Koh, J. H. Griffin, S. Filippi, A. Akay, Characterization of turbine blade friction dampers, *ASME Journal of Engineering for Gas Turbine and Power* 127 (2005) 856–862.
- [61] K. H. Koh, J. H. Griffin, Dynamic behavior of spherical friction dampers and its implication to damper contact stiffness, in: Paper GT2006-90102, Proceedings of ASME Turbo Expo 2006, May 8-11, Barcelona, Spain, 2006.
- [62] W. J. F. Govaerts, *Numerical Methods for Bifurcations of Dynamical Equilibria*, Society for Industrial and Applied Mathematics Philadelphia, PA, USA, 1990.
- [63] T. F. C. Chan, H. B. Keller, Arc-length continuation and multi-grid techniques for nonlinear elliptic eigenvalue problems, *Society for Industrial and Applied Mathematics* 3 (1982) 173–194.
- [64] M. A. Crisfield, A fast incremental iterative solution procedure that handles snap-through, *Computers and Structures* 13 (1981) 55–62.
- [65] Y. A. Kuznetsov, *Elements of Applied Bifurcation Theory*, Springer, 1998.
- [66] G. Engdahl, Chapter 1—Physics of giant magnetostriction, in: G. Engdahl (Ed.), *Handbook of Giant Magnetostrictive Materials*, Electromagnetism, Academic Press, San Diego, 2000, pp. 1–125.
- [67] C. MacWilliam, Design of a magnetostrictive actuator, Ph.D. thesis, School of Engineering and Industrial Design, University of Western Sydney (2004).
- [68] J. P. Joule, On a new class of magnetic forces, *Annals Electric Magn Chem* 8 (1842) 219–224.
- [69] W. F. Barrett, On the alterations in the dimensions of the magnetic metals by the act of magnetization, *Nature* 26 (1882) 585–586.
- [70] H. Nagaoka, K. Honda, Magnetization and magnetostriction of nickel steels, *Journal de Physique* 3 (1904) 613–620.

- [71] E. Villari, Intorno alle modificazioni del momento magnetico di una verga di ferro e di acciacom, prodotte par la trazione della medisma e pel passaggio di una corrente attraverso la stessa, *Nouvo Cimento* 20 (1864) 317–362.
- [72] L. JingHua, J. ChengBao, X. HuiBin, Giant magnetostrictive materials, *Science China Technological Sciences* 55 (2012) 1319–1325.
- [73] M. J. Dapino, F. T. Calkins, A. B. Flatau, Measured Terfenol-D material properties under varied applied magnetic field levels, in: *SPIE Symposium on Smart Structures and Materials*, 1996.
- [74] F. T. Calkins, A. B. Flatau, Transducer based measurements of Terfenol-D material properties, in: *In Proc. of SPIE Smart Structures and Materials*, Vol. 2717, 1996, pp. 709–719.
- [75] R. Kellogg, A. Flatau, Blocked force investigation of a Terfenol-D transducer, in: *Proc. SPIE, Symposium on Smart Structures and Materials*, 1999.
- [76] A. G. Olabi, A. Grunwald, Design and application of magnetostrictive materials, *Materials and Design* 29 (2008) 469–483.
- [77] F. T. Calkins, A. B. Flatau, M. J. Dapino, Overview of magnetostrictive sensor technology, *Journal of Intelligent Material Systems and Structures* 18 (2007) 1057–1066.

BIBLIOGRAPHY

Part II

APPENDED PAPERS A-D

